Bachelor thesis

Asymmetric electrode micropumps

Morten Arnoldus - s001604

Michael Hansen - s991279

ii

Contents

List of Figures

List of Tables

List of symbols

Symbol	Description	Unit
A	Area	m^2
c_i	Molar concentration of i´th species	$mol\ m^{-3}$
C	Capacitance	F
C_D	Capacitance of Debye layer	F
C_{DL}	Capacitance of the Debye layer above the large electrode	F
C_{DS}	Capacitance of the Debye layer above the small electrode	F
C_s	Intrinsic capacitance of an electrode	F
e	Elementary charge	1.602×10^{-19} C
d	Inner diameter of a tube	m
E	Electrical field	$V\ m^{-1}$
E_{young}	Youngs modulus	$N\ m^2$
F	Force	N
F_a	Faradays constant	96472.44 C mol^{-1}
F_{el}	Electrical force	N
h	Height of microfluidic channel	m
G	Width of gap between electrodes	m
J	Current density	$A\ m^{-2}$
k	Aspect ratio between the widths of the large and the small electrode	
k_B	Boltzmann constant	1.381×10^{-23} J K^{-1}
L	Width of large electrode	m
$L_{channel}$	Length of microfluidic channel	m
L_{trap}	Side length of trapezoid	m
n_i	Relative concentration of i´th species	
N_A	Avogadros number	6.022×10^{23} mol^{-1}
N	Number of electrode pairs on a single chip	
p	Pressure	Pa
q	Measure of the periodicity of electrode pairs	
Q	Flow rate	$m^3\ s^{-1}$
R	Electrical resistance	Ω

R_{hyd}	Hydraulic resistance	Pa s m^{-3}
S	Width of small electrode	m
t	Time	s
T	Temperature	K
u	Distance of bending of glass	m
v	Velocity	m s^{-1}
v_{DL}	Velocity of liquid above the large electrode	m s^{-1}
v_{DS}	Velocity of fluid above the small electrode	m s^{-1}
v_{ave}	Average velocity of liquid above an electrode	m s^{-1}
v_{slip}	Slip velocity	m s^{-1}
$\mathbf{v}$	Velocity vector	m s^{-1}
V_{ext}	Externally applied voltage	V
V	Electrical voltage	V
z_i	Number of charges of i´th species	
Z	Impedance	Ω
γ	Conductance	Ω^{-1} m^{-1}
δ_{C}	Non dimensional measure of capacitance	
ϵ	Dielectric constant	C V^{-1} m^{-1}
ζ	Zeta potential	V
η	Viscosity	kg m^{-1} s^{-1}
θ	Phase difference	rad
λ_D	Debye length	m
μ_i	Chemical potential	J
$\mu_i^{(0)}$	Standard chemical potential	J
ξ	Parameterization of position on the y axis	m
π	Pi	3.14159...
ρ	Charge density	C m^{-3}
ϱ	Resistivity	Ω m
σ	Surface charge density	C m^{-2}
ϕ	Phase angle	rad
φ	Electrical potential	V
φ_{s}	Potential just outside the Debye layer	V
ω	Angular frequency	s^{-1}
ω_0	Optimal angular frequency	s^{-1}

Chapter 1

Introduction

The motivation for fabricating micro scale devices capable of pumping liquid, is the need for driving samples through lab-on-a-chip systems. These systems promise fast, portable, low chemical consuming and cost-efficient analysis of samples. Different methods of pumping are being investigated, among others electroosmotic pumps. AC induced fluid flow above electrodes embedded in liquid has been observed by Ramos *et al.* [3]. This was done by using symmetric electrodes, and no net flow was obtained. Recently, Armand Ajdari [1] proposed a micropump based on AC driven electrode arrays. The subject was investigated by Brown *et al.* [2], who empirically demonstrated the pumping effect.

The type of micropump investigated in this thesis is based on asymmetric electrode arrays, consisting of pairs of large and small electrodes, separated by a gap. An AC potential of V is applied between the two electrodes, setting -V on the large electrode, and +V on the small electrode. This results in an electrical field and to the formation of a Debye layer above the electrode surfaces. Ions migrate from the Debye layer above one electrode to the other along arcs following the field lines as shown in Fig. 1.1. Due to longer paths and thus greater resistance in the liquid of the outer arcs of the field, the Debye layers are charged fast near the gap, leading to a gradient of charge along each of the electrodes. This gradient results in the formation of an electrical field E, which affects the ions in the Debye layer with a Coulomb force F_C as seen in Fig. 1.1(a). The ions are driven along the electrode surface away from the gap dragging the liquid along, resulting in a flow.

When the polarity of the potential is inverted, it results in two things. The reversal of the current of ions, and the reversal of the direction of the electrical field. Due to the interchanged polarity of the ions, the direction of the flow, will still be away from the electrode gap as seen in Fig. 1.1(b).

The concentration of field lines at the small electrode will be much greater than at the large electrode, resulting in a stronger electrical field. The velocity of the ions above the small electrode is therefore greater than above the large electrode. Above the small electrode, the ions will quickly dissipate, thus cancelling the electrical field. Above the large electrode this effect is not dominant, and a net flow will be formed, going from the small to the large electrode.
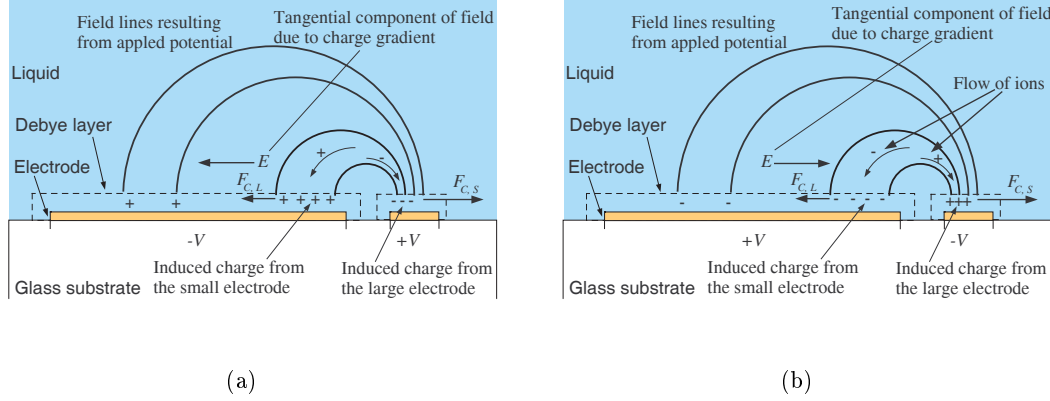
Figure 1.1: Cross section of a single pair of electrodes. (a) The situation of the system when there is a potential of -V on the large electrode, and +V on the small electrode. The potential causes an exchange of ions between the Debye layers above the electrodes. (b) The polarity of the potential has been inverted, thus reversing the flow of ions.

This effect can be taken advantage of by making arrays of electrode pairs to obtain a pumping effect, though it should be noted that this pump can only be used to drive liquids that contain at least a minimum amount of ions.

A micropump based on this effect has several advantages compared to other microfluidic pumps. It operates at voltages up to 2 V, and it is suspected to be less dependent on the concentration of charge carriers in the liquid than electroosmotic pumps. It is capable of pumping liquid containing large molecules or particles, where an electroosmotic pump would be blocked by such particles. The ability to handle large particles or molecules enables this kind of pump to be integrated with a fluidic dye laser, as the electrode micropump will be able to deal with the rhodamine molecules used by such a laser [9]. The micropump is however not capable of delivering as high pressures or flow rates as an electroosmotic pump.

The micropump investigated in this project will have a low channel height compared to the spacing between the electrode pairs, in order to improve the pressure capacity if the pump. In the empirical studies by Brown *et al.* the channel height was large compared to the spacing between the electrodes and could therefore not be used as a pump. The study of the asymmetric electrode micropump in a low channel is still an unknown territory.

This thesis investigates the theoretical background for asymmetric electrode based micropumps. The subject is also empirically investigated by designing, producing and attempting to characterize such pumps. Finally an assessment of the chip design, fabrication process and the problems encountered is given, followed by a presentation of recommended improvements. Thus, the project is very ambitious in trying to use a newly discovered mechanism for constructing a prototype pump.

The structure of the report is as follows:

Theory The theoretical background for asymmetric based pumping devices is presented. The general theory is followed by a theoretical model for the flow generated by an asymmetric electrode micropump.

Design Considerations on the design of the micropump are discussed, and in the end of the chapter, the final design is presented.

Fabrication The chapter covers the fabrication process, and the important parameters used in the fabrication. An assessment of the fabrication processes is given.

Measurements The development of an efficient setup for measurements is described. The chapter contains the results obtained in the experiments.

Summary of problems and improvements The problems encountered in the project are summarized and proposals for improvements are made.

Chapter 2

Theory

2.1 The Debye layer in equilibrium

If we consider a charged wall, the charged surface will attract ions of the opposite charge. This leads to the formation of an electrical double layer called the Debye layer consisting of an inner layer and an outer layer. The inner layer is fixed to the wall due to electrical forces, while the outer layer is mobile. It is possible to influence the outer layer by applying an external electrical force. The thickness of the Debye-layer, λ_D, is governed by the balance between these two forces. For an ionic solution in equilibrium the electrical and the diffusive forces balance each other. The thickness of the Debye layer is called the Debye length and is a characteristic scale for the electrical screening. The chemical potential is given by

$$\mu_i = \mu_i^{(0)} + kT \ln n_i + z_i e \varphi, \tag{2.1}$$

at the concentration, n_i, where, $\mu_i^{(0)}$ is the standard chemical potential. In order to determine the Debye length, λ_D, it is required that μ_i is constant, which is the same as requiring that

$$\nabla \bar{\mu}_i = 0 \Rightarrow \frac{kT}{n_i} \nabla n_i + z_i e \nabla \varphi = 0. \tag{2.2}$$

Together with Poissons equation

$$\nabla^2 \varphi = -\frac{ze}{\epsilon}(n_+ - n_-) \tag{2.3}$$

where ϵ is the permittivity of the liquid, this yields

$$\varphi(x) = \zeta e^{-\frac{x}{\lambda_D}} \tag{2.4}$$

and by using the Debye-Huckel approximation, $\frac{z_i \varphi}{kT} \ll 1$, which means that the applied voltage is much smaller than the thermal energy, it is possible to find the Debye length as

$$\lambda_D = \sqrt{\frac{\epsilon kT}{2e^2 z^2 c}}. \tag{2.5}$$

This solution is only correct for a liquid with two types of ions, $+ze$ and $-ze$. The thickness of the Debye layer is dependent on the temperature, the concentration c, and the valence number of the ions. The capacitance of the Debye layer is

$$C_{\mathrm{D}} = \frac{\epsilon}{\lambda_{\mathrm{D}}}. \tag{2.6}$$

2.2   Electroosmotic effect

The electroosmotic effect is based on the presence of an electrical double layer, i.e., the Debye layer. When the surface becomes charged, a surplus of ions of the opposite charge is left in the liquid. These ions tend to concentrate near the Debye layer, leaving the bulk of the liquid charge neutral. If an external electric field E, is applied, it will be able to pull the charged layer in the liquid along the channel. The electric force per volume is given by

$$F_{el} = \epsilon \nabla^2 \varphi E. \tag{2.7}$$

The electric force sets the liquid into motion. If no pressure gradient are present, the flow velocity can be found from the steady state Navier Stokes equation

$$\nabla^2 (\mathbf{v} + \frac{\epsilon}{\eta} \varphi E) = 0, \tag{2.8}$$

the velocity, $\mathbf{v}$ is

$$\mathbf{v} = \frac{\epsilon E}{\eta} (\varphi - \zeta). \tag{2.9}$$

When $\sigma_{\mathrm{D}} = C_{\mathrm{D}} \zeta = \frac{\epsilon}{\lambda_{\mathrm{D}}} \zeta$, the slip velocity just outside the Debye layer is

$$v_{\mathrm{slip}} = \frac{\lambda_{\mathrm{D}}}{\eta} \sigma_{\mathrm{D}} E. \tag{2.10}$$

The two first sections 2.1 and 2.2 has been inspired by the master thesis of Anders Brask [10].

2.3   Time dependent perturbation

Armand Ajdari has published a paper [1], where he states that it is possible to generate a flow using asymmetric electrodes and an AC-voltage source. The article is written in a very compact language, four pages including pictures and references, and we have spent some time to fill in the missing details.

   A simple model of the pump is considered. The model consists of a planar surface, a Debye layer and an external voltage source, as shown Fig. 2.2. In our model we have a coordinate system where the y-axis is parallel to the surface, and the x-axis is perpendicular to the surface. An AC-voltage V_{ext}, is applied to the surface of the electrodes, and taking into account the intrinsic capacitance C_{s}, of the surface as well as the surface charge density
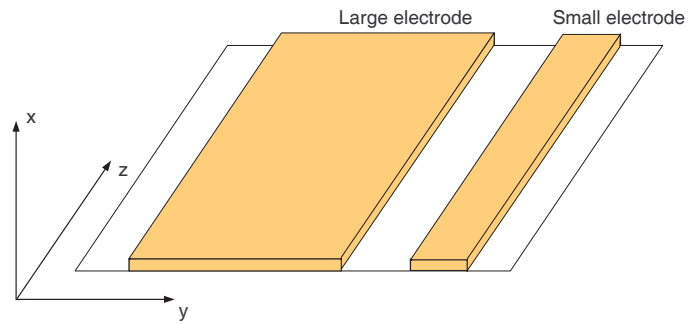
Figure 2.1: Three dimensional view of two electrodes and definition of the three axis.
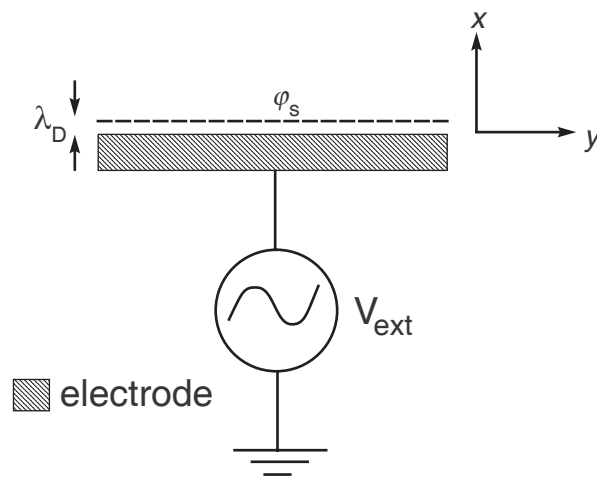
Figure 2.2: A scematic view of the simple model used in the theory. The y-axis is parallel to the surface of the electrode and the x-axis is perpendicular to the surface. The dashed line represents the Debye-layer.

σ_D, we know that the potential φ_s, on the outside of the Debye layer is related to V_{ext} by the intrinsic capacitance and the Debye layer capacitance C_D in series,

$$\varphi_s - V_{ext} = (C_s^{-1} + C_D^{-1})\sigma_D = (1 + \delta)\frac{\lambda_D \sigma_D}{\epsilon}, \tag{2.11}$$

where $\delta_c = \frac{C_D}{C_s}$ is a nondimensional measure of the electrode capacitance and $C_s + C_D = C = \frac{\epsilon}{\lambda_D(1+\delta_c)}$ is the total capacitance per area. In the model the potential, $\varphi(x, y)$, is defined in two places. At the surface of the electrode where it is V_{ext} and just outside of the Debye layer where it is φ_s. This can be formulated as

$$\varphi(0, y) = V_{ext}(y), \tag{2.12a}$$
$$\varphi(\lambda_D, y) = \varphi_s(y). \tag{2.12b}$$

Both $V_{ext}(y)$ and $\varphi_s(y)$ are dependent of y, but they do not depend on x. We imagine that the electrode is infinite in the y-direction. Away from the Debye layer, in the x-direction, the potential is weakened with the condition $\varphi(x, y) \to \varphi(\lambda_D, y)$. The AC-voltage at the electrode is given by a simple harmonic wave

$$V_{ext}(y) = V_0 \cos(qy)e^{i\omega t}, \tag{2.13}$$

where ω is the angular frequency. Outside the Debye layer, i.e., for $x > \lambda_D$ the charge density is zero and the potential $\varphi(x, y)$ must fulfill the Laplace equation

$$\bigtriangledown^2 \varphi(y) = 0. \tag{2.14}$$

Moreover, due to the wave form given by Eq. (2.13), we have $\varphi(x, y) \propto \cos(qy)e^{i\omega t}$. To satisfy Eq. (2.14) we obtain

$$\varphi(x, y) \propto \cos(qy)e^{-qx}e^{i\omega t}. \tag{2.15}$$

The change $\dot{\sigma}_D$, in surface charge σ_D, equals the current $\mathbf{J} = \sigma\mathbf{E}$, to the surface. We are only interested in the perpendicular contribution, i.e., we make an approximation where we only take the perpendicular contribution into consideration, thus $J_x = \sigma E_x$. This yields

$$\left. \begin{array}{l} \dot{\sigma}_D = \sigma\frac{\partial\varphi(y)}{\partial x} \\ \sigma_D = C\varphi_s(y) - V_{ext}(y) \end{array} \right\} \quad \Rightarrow \quad \frac{\sigma}{C}\frac{\partial\varphi(x, y)}{\partial x} = \dot{\varphi}_s(y) - \dot{V}_{ext}(y). \tag{2.16}$$

Inserting Eq. (2.15) in Eq. (2.16) we obtain

$$\frac{\sigma}{C}-q\varphi_s(y) = i\omega\varphi_s(y) - i\omega V_{ext}(y) \tag{2.17}$$

and thus

$$\varphi_s(y)\left(\frac{\sigma q}{c} + i\omega\right) = i\omega V_{ext}(y) \tag{2.18}$$

$$\varphi_s(y) = \frac{i\omega}{\omega^* + i\omega}V_{ext}(y) \tag{2.19}$$

where $\frac{\sigma q}{C} = \omega^*$. The surface charge density σ_{D}, can be expressed as

$$
\begin{aligned}
\sigma_{\mathrm{D}} &= C\big[\varphi_{\mathrm{s}}(y) - V_{\mathrm{ext}}(y)\big] \\
&= -\frac{\sigma q V_0}{\omega^* + i\omega} \cos(qy)e^{i\omega t}.
\end{aligned}
\tag{2.20}
$$

We can also determine E_y from $E_y = -\partial\varphi(y)$ and obtain

$$
E_y = \frac{-i\omega q}{\omega^* + i\omega} V_0 \sin(qy)e^{i\omega t}.
\tag{2.21}
$$

The fluid can be set into motion by electro-osmosis. The liquid is dragged by the electrical field in the liquid. There is a no slip condition on the wall of the chip and therefore the velocity changes rapidly from zero to v_{slip} just outside the Debye layer. We want to find v_{slip}. It is known from [7] that if $j(t) = j_0 e^{i\omega t}$ and $g(t) = g_0 e^{i\omega t}$ then

$$
\langle \mathrm{Re}\,[j]\mathrm{Re}\,[g]\rangle = \frac{1}{2}\mathrm{Re}\,[j^* g],
\tag{2.22}
$$

where $\langle\ldots\rangle$ means the time average. We may use this knowledge to find the time averaged v_{slip}

$$
\begin{aligned}
\langle v_{\mathrm{slip}}\rangle &= \left\langle \frac{\lambda_{\mathrm{D}}\sigma_{\mathrm{D}}}{\eta} E_y \right\rangle \\
&= \frac{\lambda_{\mathrm{D}}}{2\eta}\mathrm{Re}\,\big[\sigma_{\mathrm{D}}^{*(0)} E_y^{(0)}\big] \\
&= \frac{\lambda_{\mathrm{D}}\sigma q^2 V_0^2}{4\eta}\sin(2qy)\mathrm{Re}\left[\frac{i\omega}{\omega^{*2} + \omega^2}\right] \\
&= 0.
\end{aligned}
\tag{2.23}
$$

Unfortunately this does not reveal anything about the slip velocity. Therefore we apply perturbation theory by introducing some small dimensionless parameter $\beta \ll 1$. The potential φ and the surface density become

$$
\begin{aligned}
\varphi &= \varphi^{(0)} + \beta\varphi^{(1)} + \ldots, \tag{2.24} \\
\sigma_{\mathrm{D}} &= \sigma_{\mathrm{D}}^{(0)} + \beta\sigma_{\mathrm{D}}^{(1)} + \ldots, \tag{2.25}
\end{aligned}
$$

and to the first order in β the time averaged v_{slip} becomes

$$
\begin{aligned}
\langle v_{\mathrm{slip}}\rangle &= \left\langle \frac{\lambda_{\mathrm{D}}}{\eta}\sigma_{\mathrm{D}}\partial_y\varphi \right\rangle \\
&= \frac{\lambda_{\mathrm{D}}}{\eta}\left\langle \sigma_{\mathrm{D}}^{(0)}\partial_y\varphi^{(0)} + \beta\left(-\partial_y\varphi^{(0)}\sigma_{\mathrm{D}}^{(1)} + \partial_y\varphi^{(1)}\sigma_{\mathrm{D}}^{(0)}\right)\right\rangle.
\end{aligned}
\tag{2.26}
$$

We need to find φ^1 and σ_{D}^1 in order to determine v_{slip}. We now consider a specific choice of the spatial variation of δ_c

$$
\delta_c(y) = \delta_0\big[1 + \beta\cos(2qy + \theta)\big],
\tag{2.27}
$$

where θ is the frequency dependent phase. φ and σ_D are defined in Eqs. (2.24) and (2.25). $\varphi^{(0)}$ and $\sigma_D^{(0)}$ are the same as before, so Eq. (2.16) now reads

$$\frac{\sigma}{c}\frac{\partial}{\partial x}(\varphi^{(0)} + \beta\varphi^{(1)} + ...) = \dot{\varphi}_s^{(0)} + \beta\dot{\varphi}_s^{(1)} + ... - \dot{V}_{\text{ext}}, \tag{2.28}$$

where

$$\frac{1}{c} = (1+\delta)\frac{\lambda_D}{\epsilon} = 1 + \delta_0\big[1 + \beta\cos(2qy+\theta)\big]\frac{\lambda_D}{\epsilon}. \tag{2.29}$$

Inserting Eq. (2.29) into Eq. (2.28)

$$\frac{\lambda_D\sigma}{\epsilon}\Big(1 + \delta_0\big[1 + \beta\cos(2qy+\theta)\big]\Big)\left(\frac{\partial\varphi^{(0)}}{\partial x} + \beta\frac{\partial\varphi^{(1)}}{\partial x} + ...\right)$$
$$= \dot{\varphi}^{(0)} + \beta\dot{\varphi}^{(1)} + ... - \dot{V}_{\text{ext}} \tag{2.30}$$

the solution to the zeroth order is

$$\frac{\partial\varphi^{(0)}}{\partial x} = -q\varphi^{(0)}. \tag{2.31}$$

We collect the terms of β to the first order,

$$\big[\sigma\delta_0\cos(2qy+\theta)\big]\frac{\partial\varphi^{(0)}}{\partial x} + \sigma\left(1 + \delta_0\frac{\partial\varphi^{(1)}}{\partial x}\right) = \frac{\epsilon}{\lambda_D}\dot{\varphi}^{(1)}, \tag{2.32}$$

in short we write

$$\varphi^{(0)} = \frac{i\omega}{\omega^* + i\omega}V_0\cos(qy)e^{-qx}e^{i\omega t} \equiv \widetilde{\varphi}^{(0)}\cos(qy)e^{-qx}e^{i\omega t}. \tag{2.33}$$

Inserting Eq. (2.33) into Eq. (2.32) yields

$$-\sigma\delta_0 q\cos(2qy+\theta)\cos(qy)e^{-qx}\widetilde{\varphi}^{(0)}e^{-\omega t} + \sigma(1+\sigma_0)\frac{\partial\varphi^{(1)}}{\partial x} = \frac{\epsilon}{\lambda_D}\dot{\varphi}^{(1)}. \tag{2.34}$$

We reformulate the cosine terms to obtain

$$\cos(2qy+\theta)\cos(qy) = \frac{1}{4}\big(e^{i(2qy+\theta)} + e^{-i(2qy+\theta)}\big)\big(e^{iqy} + e^{-iqy}\big)$$
$$= \frac{1}{2}\cos(qy+\theta) + \frac{1}{2}\cos(3qy+\theta). \tag{2.35}$$

We can conclude that $\varphi^{(1)}$ contains terms proportional to $\cos(qy+\theta)$ and $\cos(3qy+\theta)$. We are now able to make a qualified guess on the solution to $\varphi^{(1)}$

$$\varphi^{(1)} = \big[A_1\cos(qy+\theta) + A_3\cos(3qy+\theta)\big]e^{i\omega t}e^{-qx}. \tag{2.36}$$

From Eq. (2.34) we can not require that $\nabla^2 \varphi^{(1)} = 0$. Using the notation from Eq. (2.36) in Eq. (2.34)

$$
\begin{aligned}
-\sigma \delta_0 q e^{-qx} \widetilde{\varphi}^{(0)} &\left[\frac{1}{2} \cos(qy + \theta) + \frac{1}{2} \cos(3qy + \theta) \right] + \sigma(1 + \delta_0) \cdot \\
&\left[-qA_1 \cos(qy + \theta) e^{-qx} - qA_3 \cos(3qy + \theta) e^{-qx} \right] e^{i\omega t} \\
&= \frac{\epsilon}{\lambda_D} i\omega \left[A_1 \cos(qy + \theta) e^{-qx} + A_3 \cos(3qy + \theta) e^{-qx} \right] e^{i\omega t}.
\end{aligned}
\tag{2.37}
$$

Collecting terms of equal harmonics yields

$$
A_1 = -\frac{1}{2} \frac{\sigma \delta_0 q \widetilde{\varphi}^{(0)}}{i\omega \frac{\epsilon}{\lambda_D} + \sigma(1 + \delta_0)q},
\tag{2.38a}
$$

$$
A_3 = -\frac{1}{2} \frac{\sigma \delta_0 q \widetilde{\varphi}^{(0)}}{i\omega \frac{\epsilon}{\lambda_D} + \sigma(1 + \delta_0)q}.
\tag{2.38b}
$$

We are now able to find $\varphi^{(1)}$ and thereby $E_y^{(1)}$

$$
\varphi^{(1)} = \frac{\sigma \delta_0 q \widetilde{\varphi}^{(1)}}{i\omega \frac{\epsilon}{\lambda_D} + q\sigma(1 + \delta_0)} \left[\frac{1}{2} \cos(qy + \theta) + \frac{1}{2} \cos(3qy + \theta) \right] e^{i\omega t} e^{-qx}.
\tag{2.39}
$$

We now introduce

$$
\omega^* = (1 + \delta_0) \frac{\lambda_D}{\epsilon} \sigma q,
\tag{2.40}
$$

then $\varphi^{(1)}$ becomes

$$
\begin{aligned}
\varphi^{(1)} &= \frac{\sigma \delta_0 q V_0}{i\omega \frac{\epsilon}{\lambda_D} + q\sigma(1 + \delta_0)\delta_0} \frac{i\omega}{\omega^* + i\omega} \frac{1}{2} \left[\cos(qy + \theta) + \cos(3qy + \theta) \right] e^{i\omega t} e^{-qx} \\
&= -\frac{i\omega \delta_0 q \sigma V_0}{(\omega^* + i\omega)^2} \frac{\lambda_D}{2\epsilon} \left[\cos(qy + \theta) + \cos(3qy + \theta) \right] e^{i\omega t} e^{-qx}
\end{aligned}
\tag{2.41}
$$

and $E_y^{(1)}$ is

$$
E_y^{(1)} = \frac{i\omega}{(\omega^* + i\omega)^2} \delta_0 q^2 \sigma V_0 \frac{\lambda_D}{2\epsilon} \left[\cos(qy + \theta) + \cos(3qy + \theta) \right] e^{i\omega t} e^{-qx}.
\tag{2.42}
$$

The equation for σ_D is

$$
\sigma_D = c(\varphi_s - V_{ext}).
\tag{2.43}
$$

We insert Eqs. (2.29) and (2.24) in Eq. (2.43)

$$
\frac{\lambda_D}{\epsilon} \left(1 + \delta_0 \left[1 + \beta \cos(2qy + \theta) \right] \right) (\sigma_D^{(0)} + \beta \sigma_D^{(1)} + ...) = \varphi^{(0)} + \beta \varphi^{(1)} + ... - V_{ext}.
\tag{2.44}
$$

Only terms in β of the first order are of interest

$$
\frac{\lambda_D}{\epsilon} \sigma_D \cos(2qy + \theta) \sigma_D^{(0)} + \frac{\lambda_D}{\epsilon} (1 + \delta_0) \sigma_D^{(1)} = \varphi^{(1)}.
\tag{2.45}
$$

Inserting $\sigma_{\mathrm{D}}^{(0)}$ and Eq. (2.36) yields

$$\frac{\lambda_{\mathrm{D}}}{\epsilon}\delta_0\frac{-q\sigma V_0}{\omega^* + i\omega}e^{i\omega t}\cos(2qy+\theta)\cos(qy) + \frac{\lambda_{\mathrm{D}}}{\epsilon}(1+\delta_0)\sigma_{\mathrm{D}}^{(1)} \quad = -\frac{\sigma\delta_0 V_0 i\omega e^{i\omega t}}{\frac{\epsilon}{\lambda_{\mathrm{D}}}(i\omega + \omega^*)^2}\cos(2qy+\theta)\cos(qy),$$
$$(2.46)$$

notice that the cosine terms has been rewritten. We are now able to determine $\sigma_{\mathrm{D}}^{(1)}$

$$\sigma_{\mathrm{D}}^{(1)} = \frac{\omega^*}{(\omega^* + i\omega)^2}\frac{\delta_0}{\delta_0 + 1}\sigma q V_0 \frac{1}{2}\left[\cos(qy+\theta) + \cos(3qy+\theta)\right]e^{i\omega t}. \qquad (2.47)$$

We are now able to deduce an expression for v_{slip} by using Eq. (2.47) and Eq. (2.42). In Eq. (2.23) we have seen that the zero order solution to v_{slip} is zero, and by reducing Eq. (2.26) to the first order we get

$$v_{\mathrm{slip}} = \beta\frac{\lambda_{\mathrm{D}}}{\eta}\langle E_y^{(0)}\sigma_{\mathrm{D}}^{(1)} + E_y^{(1)}\sigma_{\mathrm{D}}^{(0)}\rangle, \qquad (2.48)$$

which can be rewritten due to Eq. (2.22) to

$$v_{\mathrm{slip}} = \beta\frac{\lambda_{\mathrm{D}}}{2\eta}\left(\mathrm{Re}\left[E_y^{*(0)}\sigma_{\mathrm{D}}^{(1)}\right] + \mathrm{Re}\left[E_y^{*(1)}\sigma_{\mathrm{D}}^{(0)}\right]\right). \qquad (2.49)$$

We can know conclude that

$E_y^{(0)}$ varies with $\sin(qy)$,

$E_y^{(1)}$ varies with $\sin(qy+\theta)$ and $\sin(3qy+\theta)$,

$\sigma_{\mathrm{D}}^{(0)}$ varies with $\cos(qy)$,

$\sigma_{\mathrm{D}}^{(1)}$ varies with $\cos(qy+\theta)$ and $\cos(3qy+\theta)$.

We find the spatially constant terms

$$\cos(qy+\theta)\sin(qy) = \frac{1}{2}\sin(2qy+\theta) - \frac{1}{2}\sin(\theta), \qquad (2.50)$$

$$\sin(qy+\theta)\cos(qy) = \frac{1}{2}\sin(2qy+\theta) + \frac{1}{2}\sin(\theta), \qquad (2.51)$$

$$3\cos(3qy+\theta)\sin(qy) = \frac{3}{2}\sin(4qy+\varphi) - \frac{3}{2}\sin(2qy+\theta), \qquad (2.52)$$

$$3\sin(3qy+\theta)\cos(qy) = \frac{3}{2}\sin(4qy+\varphi) + \frac{3}{2}\sin(2qy+\theta). \qquad (2.53)$$

The only spatially constant terms are in Eq. (2.50) and Eq. (2.51). All other terms can be neglected in the calculation of v_{slip}.

We start by calculating the first product in Eq. (2.49)

$$E_y^{(0)} = \frac{i\omega}{\omega^* + i\omega} qV_0 \sin(qy)e^{i\omega t} \tag{2.54}$$

$$\sigma_D^{(1)} = \frac{\omega^*}{(\omega^* + i\omega)^2}\frac{\delta_0}{\delta_0 + 1}\sigma qV_0\frac{1}{2}\left(\cos(qy + \theta) + 3\cos(3qy + \varphi)\right)e^{i\omega t}. \tag{2.55}$$

Now we can determine the contribution of the first product to v_{slip}. We only include the spatially constant terms of the cosine and sine product

$$\langle v_{\text{slip}}\rangle = \frac{\lambda_D}{2\eta}\text{Re}\left[E_y^{(0)*}\sigma_D^{(1)}\right]$$

$$= \frac{\lambda_D}{2\eta}\frac{\delta_0}{\delta_0 + 1}\sigma q^2 V_0^2\frac{-1}{4}\sin(\theta)\text{Re}\left[\frac{-i\omega}{\omega^* + i\omega}\frac{\omega^*}{(\omega^* + i\omega)^2}\right]$$

$$= \frac{-\lambda_D}{8\eta}\sigma V_0^2 q\sin(\theta)\frac{\delta_0}{(\delta_0 + 1)^2}\left(\frac{\omega}{\omega^*} + \frac{\omega^*}{\omega}\right)^{-2}. \tag{2.56}$$

The second product in Eq. (2.49) contains

$$E_y^{(1)} = \frac{i\omega}{(\omega^* + i\omega)^2}\delta_0\sigma q^2 V_0\frac{\lambda_0}{\epsilon}\frac{1}{2}\left(\sin(qy + \theta) + 3(3qy + \theta)\right)e^{i\omega t}, \tag{2.57}$$

$$\sigma_D^{(0)} = -\frac{\sigma qV_0}{\omega^* + i\omega}\cos(qy)e^{i\omega t}. \tag{2.58}$$

When determining the contribution of the second products to v_{slip}, we only include the spatially constant terms of the cos-sine product

$$\langle v_{\text{slip}}\rangle = -\frac{\lambda_D}{2\eta}\text{Re}\left[E_y^{(1)*}\sigma_D^{(0)}\right]$$

$$= -\frac{\lambda_D}{2\eta}\sigma^2 q^3 V_0^2\frac{\delta_0}{4}\frac{\lambda_D}{\epsilon}\sin(\theta)\text{Re}\left[\frac{-i\omega}{(\omega^* - i\omega)^2}\frac{1}{\omega^* + i\omega}\right]$$

$$= \frac{\epsilon}{8\eta}\frac{\delta_0}{(\delta_0 + 1)^2}V_0^2 q\sin(\theta)\left(\frac{\omega}{\omega^*} + \frac{\omega^*}{\omega}\right)^{-2}. \tag{2.59}$$

By combining Eqs. (2.56) and (2.59) we are able to determine v_{slip}

$$\langle v_{\text{slip}}\rangle = \frac{\delta_0}{(\delta_0 + 1)^2}\frac{\epsilon V_0^2 q}{4\eta}\sin(\theta)\left(\frac{\omega}{\omega^*} + \frac{\omega^*}{\omega}\right)^{-2}. \tag{2.60}$$

We are now able to make the following comments on the result

$v_{\text{slip}} \propto V_0^2$	The velocity grows with the square of the applied voltage.
$v_{\text{slip}} \propto q$	The velocity grows with q, $\frac{1}{q}$ is the spatial period of the electrodes.
$v_{\text{slip}} \propto \sin(\theta)$	The effect is only present for $\theta \neq 0$, i.e., the asymmetric case.
$v_{\text{slip}} \propto \epsilon$	The effect grows with the dielectric properties of the liquid.

The model should be interpreted as that the pumping effect will only take place if there is an asymmetry present in the system. The asymmetric properties of the arrays results in a phase difference between the applied voltage and the impedance of the electrodes, this leads to a pumping effect. In the model, the phase difference is given by θ. The pumping effect is inverse proportional to the spatial period of the electrode array, so the pumping effect should increase with miniaturization.
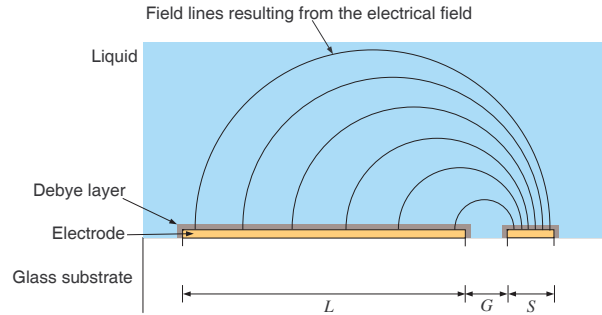
Figure 2.3: Schematic sideview of a single electrode pair on a glass substrate embedded in water. A double layer of ions has been formed near the surface of the electrodes. Semicircular electrical field lines are shown going from one electrode to the other.

2.4 A simple theoretical model for the flow of liquid

AC induced fluid flow was discovered by Ramos *et al.* [3], who investigated the symmetric case for which no net flow can be obtained. Ramos showed that the flow of the fluid above the electrodes strongly depended on the frequency of the applied potential. The flow of fluid was termed AC electroosmosis, and explained as a result of non uniform build up of charge in the Debye layers above each electrode resulting in an electrical field driving ions away from the electrodes.

Brown *et al.* [2] was inspired by the work of Ajdari [1]. He empirically showed that a net flow could be obtained, by making electrode arrays asymmetrical. He also presented a theoretical model for a system consisting of two electrodes. In the model the velocity of the fluid above each electrode is determined. This section thoroughly explains and evaluates this model.

2.4.1 The Brown model

The electrodes used in AC induced micropumping are typically of the order 2-50 μm. To make a exact model of them would require taking the behavior of the field near the ends of the electrodes into account, which would complicate the problem. Therefore the system is simplified, assuming it can be described as two infinitely long electrodes of different widths on a non-conducting substrate embedded in an aqueous solution as shown in Fig. 2.3. This assumption is justified as the length of the electrodes is much greater than the width. An AC voltage is applied to the electrodes. The amplitude of the applied potential does not exceed the ionization potential of approximately 1.2 V for water.

As explained in Sec. 2.1 a Debye layer is formed near the surface of each electrode. The Debye layer acts as a capacitor between the electrode and the bulk water. It is assumed that the frequency of the applied potential is low enough for ions to equilibrate locally, meaning that the ions does not move across the electrode surface during one cycle. If the assumption is not made, then it would be necessary to model the full, dynamical system.
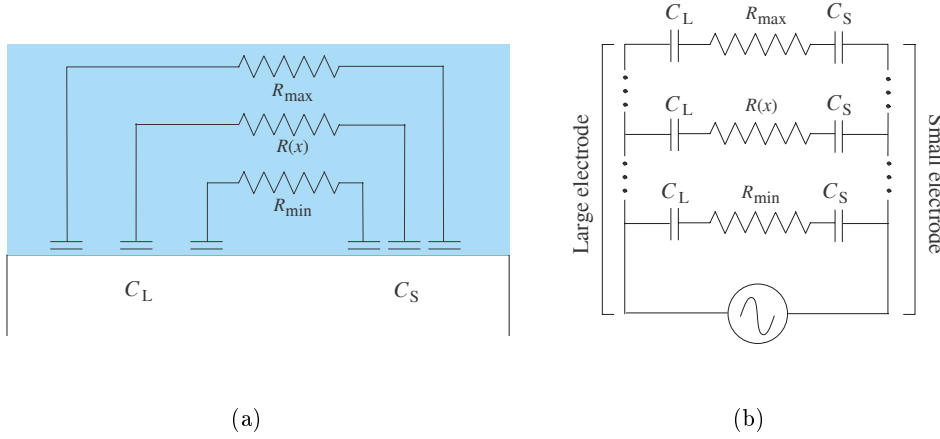
Figure 2.4: The equivalent circuit for the system of two electrodes, Debye layers, and the buffer liquid. (a) The Debye layers at the electrodes is depicted as capacitors, and the tubes from Fig. 2.3 is depicted as resistors. The resistance of the liquid varies with the length of the tube. This means that the greatest resistance $R_{\max}$ is observed at the far edges of the electrodes, and the smallest $R_{\min}$ at the near edges. The capacitance of the Debye layer at the large electrode is C_{L}, while it is C_{S} at the small electrode. (b) Serial connections of capacitors and resistors are joined in a parallel network and an AC voltage source is applied to them. Only three of such serial connections are shown, although the model should contain enough for a continuous description.

This would be a much greater task, and we only want to investigate how well this simple model can predict the behavior of the system.

When the AC voltage is applied, an electrical field will be created between the electrodes. If it is assumed that the distortion of the field near the edges of the electrodes is negligible, the resulting field lines can be approximated to be semicircular. Thus they start from one electrode and terminates on the other. The complexity of the field is reduced, allowing an analytical calculation of field parameters to be done.

It is also assumed that a current of ions will flow from one electrode to the other, following paths parallel to the field lines, due to the electrical field. The current changes the amount of charge contained in the Debye layers. The liquid is divided up into tubes parallel to the field lines, and will act as resistors due to the flow of current. Thus the system of electrodes, double layers and liquid tubes can be described by an equivalent electrical diagram consisting of capacitor-resistor-capacitor as shown in Fig. 2.4.

2.4.2 The geometry of the system

The geometry of the system must be described to allow calculation of the physical properties of the pump. Looking at Fig. 2.3 the width of the large electrode is L, the width of

Figure 2.5: The electrode pair viewed from the side. The origin of the system of reference lies between the two electrodes. The points a and b indicates the start of large and small electrode respectively.

the small electrode is S, and the size of the gap is G. We introduce the ratio between the electrode widths as

$$k = \frac{L}{S}. \tag{2.61}$$

Since $L = kS$ we want to find an origin so that

$$y = \xi \frac{1}{\sqrt{k}}, \quad \text{for} \quad y > 0 \tag{2.62a}$$

$$y = -\xi \sqrt{k}, \quad \text{for} \quad y < 0. \tag{2.62b}$$

Here we have introduced ξ, which is a parameterization of the y axis. We have also introduced the inner points, a and b, of the start of the large and small electrode respectively, as seen in Fig. 2.5. Using ξ, we can write the inner points, a and b, as

$$a = -\xi_{\mathrm{G}} \sqrt{k} \tag{2.63a}$$

$$b = \xi_{\mathrm{G}} \frac{1}{\sqrt{k}}. \tag{2.63b}$$

ξ_{G} is determined by writing the size G, of the gap as the distance from a to b

$$G = b - a = \xi_G \left(\frac{1}{\sqrt{k}} + \sqrt{k} \right) \tag{2.64}$$

yielding

$$\xi_{\mathrm{G}} = \frac{G}{\frac{1}{\sqrt{k}} + \sqrt{k}}. \tag{2.65}$$

Similarly, for the outer point $b + S$ of the small electrode

$$b + S = \xi_{\mathrm{S}} \frac{1}{\sqrt{k}}. \tag{2.66}$$

ξ_{S} is determined by combining Eq. (2.66) with Eqs. (2.64), (2.63b) and (2.65)

$$\frac{G}{k+1} + S = \xi_{\mathrm{S}} \frac{1}{\sqrt{k}} \quad \Rightarrow \quad \xi_{\mathrm{S}} = \frac{G + L + S}{\sqrt{k} + \frac{1}{\sqrt{k}}}. \tag{2.67}$$

Finally, for the outer point $a - L$ of the large electrode we get

$$a - L = -\xi_{\mathrm{L}} \sqrt{k}, \tag{2.68}$$
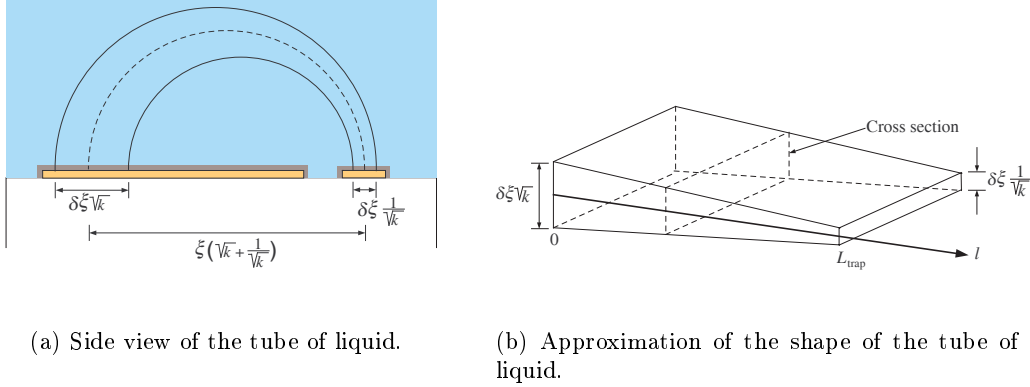
(a) Side view of the tube of liquid.

(b) Approximation of the shape of the tube of liquid.

Figure 2.6: In (a) a cross section of the tube of liquid going from the small electrode to the large is shown. In (b) we have approximated the tube of liquid with a trapezoid.

and by combining Eq. (2.68) with Eqs. (2.63a), (2.65) and (2.61) we arrive at

$$\xi_{\mathrm{L}} = \frac{G + L + S}{\sqrt{k} + \frac{1}{\sqrt{k}}}, \tag{2.69}$$

which is equal to Eq. (2.67). Thus $\xi_{\min} = \xi_{\mathrm{G}}$ indicates the start of the electrodes, while $\xi_{\max} = \xi_{\mathrm{S}} = \xi_{\mathrm{L}}$ indicates the ends of the electrodes. The introduction of ξ as a parameterization of the y axis, results in some useful properties. When ξ runs from $\xi_{\min} = \frac{G}{\frac{1}{\sqrt{k}} + \sqrt{k}}$ to $\xi_{\max} = \frac{G + L + S}{\sqrt{k} + \frac{1}{\sqrt{k}}}$ then $y = \xi \frac{1}{\sqrt{k}}$ runs from b to $b + S$ for $y > 0$, and $y = -\xi\sqrt{k}$ runs from a to $a - L$ for $y < 0$. Furthermore we note that

$$\delta y = \frac{1}{\sqrt{k}}\delta\xi, \quad \text{for} \quad y > 0, \tag{2.70a}$$

$$\delta y = -\sqrt{k}\delta\xi, \quad \text{for} \quad y < 0. \tag{2.70b}$$

With the parameterization of the y axis in place, we are now ready to describe the geometry of the electrodes. We consider Fig. 2.6(a). The tube goes from the large electrode, where it has a thickness of $\sqrt{k}\delta\xi$ to the small electrode where it has a thickness of $\frac{1}{\sqrt{k}}\delta\xi$. We want to find the thickness as a function of the position along the center line. To do this we approximate the tube with a trapezoid of infinite length in the z direction as shown in Fig. 2.6(b). The side length L_{trap} of the trapezoid is equal to the length of the centerline of the tube $L_{\mathrm{trap}} = \frac{\pi}{2}\left(\sqrt{k} + \frac{1}{\sqrt{k}}\right)\xi$. The axis l represents the center line of the tube. We now want to determine the area $A(l)$ per unit length in the z direction of a cross section of the trapezoid as a function of l. This function must be linear and because the values of

$A(0)$ and $A(L_{\text{trap}})$ are known, $A(l)$ can be written as

$$A(l) = \left[\sqrt{k} - (\sqrt{k} - \frac{1}{k})\frac{l}{L_{\text{trap}}}\right]\delta\xi. \tag{2.71}$$

2.4.3 Determining the impedance of the system

The liquid has a certain conductance γ, and therefore each tube of liquid act as a resistor as indicated in Fig. 2.4. We want to find the resistance of the tube as a function of ξ, and we use the approximation that the tube can be described as a trapezoid as mentioned above. The resistance $R(\xi)$ per unit length in the z direction of such a trapezoid filled with liquid of resistivity $\varrho = \frac{1}{\gamma}$, is

$$\begin{aligned}
R(\xi) &= \int_0^{L_{\text{trap}}} \varrho \frac{1}{A(l)} dl \\
&= \varrho \int_0^{L_{\text{trap}}} \frac{1}{\left[\sqrt{k} - (\sqrt{k} - \frac{1}{k})\frac{l}{L_{\text{trap}}}\right]w\delta\xi} dl \\
&= \frac{\varrho}{\delta\xi} \int_0^{L_{\text{trap}}} \frac{1}{A - Bl} dl,
\end{aligned} \tag{2.72}$$

where

$$A = \sqrt{k} \qquad \text{and} \qquad B = \frac{\sqrt{k} - \frac{1}{\sqrt{k}}}{L_{\text{trap}}}. \tag{2.73}$$

Continuing from Eq. (2.72), and changing the integrand from l to $s = -Bl$ yields

$$\begin{aligned}
R(\xi) &= \frac{\varrho}{\delta\xi}\frac{1}{-B} \int_0^{-BL_{\text{trap}}} \frac{1}{A + s} ds \\
&= \frac{\pi(\sqrt{k} + \frac{1}{\sqrt{k}})\xi}{2\gamma\delta\xi} \frac{\ln k}{\sqrt{k} - \frac{1}{\sqrt{k}}}.
\end{aligned} \tag{2.74}$$

The capacitance of the layer of ions above the electrode surface must be determined. Both a Stern layer and a Debye layer contributes to the capacitance. The amount of charge that can be contained in the Stern layer is limited. Therefore, it is reasonable to address the capacitance to the charge separation effect of the Debye layer.

We now assume three things. Firstly, all ions in the layer are mobile, and secondly the Debye length does not change, which is true for a given amplitude. This means that the capacitance is static. Thirdly we expect that the electrostatic energy of the ions in the Debye layer, due to the applied voltage, is negligible compared to the thermal energy. As described in Sec. 2.1, this allows use of the Debye-Hückel approximation to determine the characteristic length λ_{D} of the Debye layer. Thus the capacitance of the Debye layers above the large and small electrode is determined by

$$C_{\text{DL}} = \frac{\epsilon}{\lambda_{\text{D}}}\delta\xi\sqrt{k} \tag{2.75a}$$

$$C_{\text{DS}} = \frac{\epsilon}{\lambda_{\text{D}}}\frac{\delta\xi}{\sqrt{k}}, \tag{2.75b}$$

The total impedance Z per unit area in the z direction of a single tube, is determined by

$$Z(\xi) = Z_{\text{DL}} + R(\xi) + Z_{\text{DS}} = \frac{1}{i\omega\sqrt{k}\frac{\epsilon}{\lambda_{\text{D}}}} + \frac{\pi\xi\left(\sqrt{k} + \frac{1}{\sqrt{k}}\right)}{2\gamma}\frac{\ln k}{\sqrt{k} - \frac{1}{\sqrt{k}}} + \frac{1}{i\omega\frac{1}{\sqrt{k}}\frac{\epsilon}{\lambda_{\text{D}}}}$$

$$= \left(\sqrt{k} + \frac{1}{\sqrt{k}}\right)\left(\frac{\pi m \xi}{2\gamma} + \frac{\lambda_{\text{D}}}{i\omega\epsilon}\right), \tag{2.76}$$

where we have introduced $m = \frac{\ln k}{\sqrt{k} - \frac{1}{\sqrt{k}}}$.

2.4.4   Determining the velocity of liquid above the electrodes

The potential φ applied to the electrodes is an AC potential given by $\varphi(t) = \varphi_0 e^{i\omega t}$ oscillating at a angular frequency ω. The potential φ_{DL} across the Debye layer of the large electrode is simply

$$\varphi_{\text{DL}} = \frac{Z_{\text{DL}}}{Z}\varphi(t) = \frac{\frac{\lambda_{\text{D}}}{i\omega\epsilon}\frac{1}{\sqrt{k}}}{\left(\sqrt{k} + \frac{1}{\sqrt{k}}\right)\left(\frac{\pi m\xi}{2\gamma} + \frac{\lambda_{\text{D}}}{i\omega\epsilon}\right)}\varphi(t)$$

$$= \frac{1}{(k+1)\left(1 + \frac{i\pi\omega\epsilon m\xi}{2\gamma\lambda_{\text{D}}}\right)}\varphi(t). \tag{2.77}$$

As can be seen from Eq. (2.77), the potential across the Debye layer varies with the position on the electrode. If we recall that the electric field is the negative gradient of the potential, then this variation results in the generation of a horizontal electric field which is given by

$$E_{\text{HL}} = -\nabla\varphi_{\text{DL}}$$

$$= -\frac{\varphi(t)}{\sqrt{k}(1+k)}\frac{\frac{i\omega\epsilon\pi m}{2\lambda_{\text{D}}\gamma}}{\left(1 + \frac{\omega\epsilon\pi m\xi}{2\lambda_{\text{D}}\gamma}\right)^2}. \tag{2.78}$$

The electric field exerts a force on the ions in the double layer, causing them to move across the electrode. From Sec. 2.2 it is known that the velocity of the ions is determined by the v_{slip} condition, and thus that the speed is given by

$$v_{\text{DL}} = \frac{\lambda_{\text{D}}\sigma_{\text{DL}}E_{\text{HL}}}{\eta}. \tag{2.79}$$

The surface charge distribution σ_{DL}, of the double layer is determined by the potential across the double layer, its capacitance and the geometry of the electrodes

$$\sigma_{\text{DL}} = \varphi_{\text{DL}}\frac{\epsilon}{\lambda_{\text{D}}}. \tag{2.80}$$

Inserting (2.80) into Eq. (2.79), we get

$$v_{\text{DL}} = \frac{\epsilon}{\eta}E_{\text{HL}}\varphi_{\text{DL}}. \tag{2.81}$$

We want to find the average velocity $\langle v_{\mathrm{DL}}(\xi) \rangle$ over an entire cycle, above the large electrode as a function of the position. Since the expression for the velocity of the ions contains complex elements, we use complex theory [7] to find the average velocity

$$\langle v_{\mathrm{DL}}(\xi) \rangle = \frac{1}{2}\mathrm{Re}\left[\frac{\epsilon}{\eta}\varphi_{\mathrm{DL}}E_{\mathrm{HL}}^*\right].$$ (2.82)

Inserting expressions for φ_{DL} and the complex conjugate of E_{HL} yields

$$\langle v_{\mathrm{DL}}(\xi) \rangle = \frac{\epsilon}{2\eta}\mathrm{Re}\left[\frac{\varphi(t)}{1+k}\frac{1}{1+\frac{i\omega\epsilon\pi m\xi}{2\lambda_{\mathrm{D}}\gamma}}\frac{-\varphi^*(t)}{\sqrt{k}(1+k)}\frac{\frac{-i\omega\epsilon\pi m}{2\lambda_{\mathrm{D}}\gamma}}{\left(1-\frac{i\omega\epsilon\pi m\xi}{2\lambda_{\mathrm{D}}\gamma}\right)^2}\right].$$ (2.83)

Setting

$$p = \frac{\omega\epsilon\pi m}{2\lambda_{\mathrm{D}}\gamma} \qquad \text{and} \qquad v_{\mathrm{L0}} = \frac{\epsilon}{2\eta\sqrt{k}(1+k)^2},$$

and recalling that $\varphi(t) = \varphi_0 e^{i\omega t}$ we get

$$\langle v_{\mathrm{DL}}(\xi) \rangle = v_{\mathrm{L0}}\varphi_0^2\mathrm{Re}\left[\frac{1}{1+ip\xi}\frac{ip}{(1-ip\xi)^2}\right]$$

$$= -v_{\mathrm{L0}}\varphi_0^2\frac{p^2\xi}{\left(1+(p\xi)^2\right)^2}.$$ (2.85)

The average velocity $\langle v_{\mathrm{DS}(\xi)} \rangle$ across the small electrode is determined in the same way

$$\langle v_{\mathrm{DS}}(\xi) \rangle = -v_{\mathrm{S0}}\varphi_0^2\frac{p^2\xi}{\left(1+(p\xi)^2\right)^2},$$ (2.86)

where

$$v_{\mathrm{S0}} = -\frac{\epsilon\sqrt{k}}{2\eta\left(1+\frac{1}{k}\right)^2} \quad = -k^3 v_{\mathrm{L0}}.$$ (2.87)

To obtain the average velocity v_{ave} of the liquid above the surface of the large electrode, $\langle v_{\mathrm{DL}}(\xi) \rangle$ is integrated

$$\langle v(\xi)_{\mathrm{DL}} \rangle = \frac{\int_{-\sqrt{k}\xi_{\min}}^{-\sqrt{k}\xi_{\max}}\langle v_{\mathrm{DL}}(\xi) \rangle\sqrt{k}d\xi}{\sqrt{k}(\xi_{\max}-\xi_{\min})}.$$ (2.88)

$\langle v(\xi) \rangle$ is obtained the same way.

2.4.5 Evaluation of the Brown model

It is important to note that the model should be regarded as nothing more than an initial step to understand the behavior of the fluid flow induced by asymmetric electrodes. It should be noted that, according to the model, the velocity of the liquid above the small electrode is k^3 times larger than the velocity above the large electrode. This effect can be assigned to the fact that the electrical field at the small electrode is much larger than

above the large electrode. At first this would indicate that the flow above the small electrode dominates, but this is not the case. The model assumed that the distance the ions moved along the electrode surface during half a cycle was negligible. Some calculation will enlighten this. By using the mathematica notebook shown in Appendix A we can determine the average velocities v_{ave} above electrodes for which $L = 30\mu$m, $S = 10\mu$m and $G = 10\mu$m, for a solution of liquid with a dielectric constant of 80 $\epsilon_0 = 7.083 \times 10^{-12}$, viscosity $\eta = 1 \times 10^{-3}$ kg m^{-1} s^{-1} at frequency of 545 Hz. The ions above the large electrode will move at a speed of 160 $\frac{\mu\text{m}}{\text{s}}$ to be moved a negligible distance of 90 nm. For the small electrode, the ions will move at a speed of 4250 $\frac{\mu\text{m}}{\text{s}}$ to be moved approximately 2.3 μm, almost half across the width of the electrode. This results in the ions above the small electrode quickly dissipates, leading to a reduction of the tangential field thus that only a very little flow is induced. Then the net flow is dominated by the large electrode. Thus the flow will go from the small to the large electrode, which was empirically observed by Brown [2].

Another assumption is that the field lines are semicircular, and that current from one electrode to the other flows through tubes following these field lines. At this stage the exact behavior of the field is not known. If the height of the channel becomes too low it might cause the field lines to be pressed down against the surface, causing a more uniform charging of the Debye layers, thus leading to a reduction of the pumping effect. The model is far from complete, and further investigations into the nature of the flow of ions must be conducted if a satisfactory model of the net flow is to be presented. It would be natural to do this by simulation using FEMlab.

2.5   Determining the timescale of the system

In order to approximate how fast the charge builds up at the Debye layer, it is useful to determine a characteristic timescale τ of the system. As described previously, the system of two electrodes embedded in liquid, is equivalent to a series connection of two capacitors and a resistor. The timescale of such a system is $\tau = RC$, where $C = \frac{C_D}{2}$. The resistance of the bulk liquid is equivalent to $R = \frac{1}{\gamma}\frac{L_{\text{liquid}}}{A}$, where A and L_{liquid} is the cross sectional area and the length of the bulk liquid respectively. The capacitance is $C = \frac{\epsilon A}{L_{\text{capacitor}}}$. A is the cross sectional area of the capacitor, which is the same as the cross sectional area for the resistor. The length between the two plates of the resistor is $L_{\text{capacitor}} = 2\lambda_{\text{D}}$. Calculating the timescale yields

$$\tau = RC = \frac{L_{\text{liquid}}}{\gamma}\frac{\epsilon}{2\lambda_{\text{D}}}. \tag{2.89}$$

The characteristic time scale for the systems investigated in this project are of the order of 0.1 ms.

Chapter 3

The design of the micropump

The design process included definition of all the dimensions of the features of the pump and planning the fabrication process accordingly. We also had to decide which design was best suited for testing the pumps. The design was made in L-Edit v. 10.12 and the masks were produced by a Dutch company called DeltaMask.

3.1 Specifications and requirements

Before the design process was initiated we considered which features we wanted on the chip and we also considered what factors that could be a problem.

The pump should consist of two glass plates separated by a polymer film, in which microfluidic channels had been defined. In the bottom of the channels, electrode arrays would have been made, connected to a voltage source by two rectangular interconnection electrodes. The channels should have in- and outlets to allow introduction of liquid in them through fluid interconnections. To obtain such a chip we would first define the electrode arrays on a glass wafer. Then we would deposit a polymer film onto the wafer and define channels by using lithography and etching. The top of the channels would be closed by bonding a glass wafer on top. The final fabrication steps would consist of sawing the wafer into chips, making in- and outlets and bonding wires to the interconnection electrodes.

The process of bonding SU-8 together with PMMA is a well established technique at MIC. It has been used by several experimentalists and is also used in the fabrication of the fluidic dye laser [9]. In the future a possible application of the micropump is the integration with the fluidic dye laser, therefore it is natural to fabricate the micro pumps in a similar way.

3.2 The components of the micropump

In this section the design of the different parts of the chip will be dealt with. The three parts, the electrodes, the microfluidic channel and the interconnections are linked to each other and a change in the design of one of the parts will influence the design of the rest of the chip.
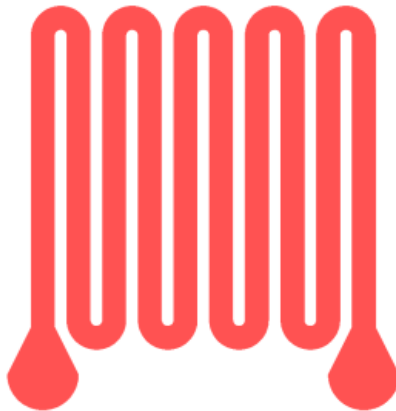
Figure 3.1: The design of the microfluidic channel. The channel has nine turns and the inlet and outlet are placed in the bottom at each end of the channel.

3.2.1   Design of the microfluidic channel

The micropump should be able to deliver relative high pressures. The pressure drop Δp, of a liquid of viscosity η in a microfluidic channel of height h, and length L_{channel} is given by

$$\Delta p = 6 v_{\text{slip}} \frac{1}{h^2} \eta L_{\text{channel}}. \tag{3.1}$$

The pressure is proportional to the length of the channel, and to the slip velocity. Furthermore it is inversely proportional to the square of the height of the channel. To obtain a large pressure, a long channel of low height is feasible. In addition, a large number of electrode pairs are placed along the channel in order to be able to build up a high pressure.

A long channel is easily made in a small area by using a meander shape as shown in Fig. 3.1. This way we could place channel 12 cm long on an area of 1.8 × 2.5 cm. The start and end of the channel needed to be at a reservoir in order to make room for the fluidic interconnections.

As mentioned in Sec. 2.4, it is possible that a small height of the channel may lead to a reduction of the pumping effect. Therefore we decided to use two different heights of the SU-8 layer to investigate how the pumping effect depends of the channel height. It had previously been reported that the pumping effect was present in high channels. If the pumping effect is also present in low channels it would imply that the micropump is capable of delivering higher pressures, as the pressure is inverse proportional to the channel height. We used two different types of SU-8 to give channel heights of 10 μm and 50 μm. The channel height is relatively low compared to the period of the electrodes. In

the experiments carried out by Brown *et al.* [4] the channel height was large compared to the period of the electrodes, he had a channel height to period ratio between five and ten. In this project the ratio will be one to ten up to one.

3.2.2 Design of the interconnections

For the chip we needed two types of interconnections, an inlet and outlet for the fluidic connections, and an access to the electrodes making it possible to connect the chip to an external power supply. For the fluidic connections we needed to make a hole in the lid of the chip. This could be done by drilling or by etching. It has previously been reported by Søren Balslev *et al.*, [9] to make the holes for the fluidic interconnections by drilling, and this method has proved to be easy and efficient. There were several ways to get access to the interconnection electrodes

1. Drilling a hole down to the gold layer.

2. Using a conducting glue through the sides of the chip.

3. Remove some of the lid, and then use a conducting glue.

4. Remove some of the lid, and then solder a wire onto the gold.

The first option had some obvious pitfalls. The drilling might damage, or completely remove the gold layer underneath the hole. Such a situation would make the chip useless. The next option was more appealing, but we where not sure that we could get the glue in between the bottom glass plate and the lid. In the worst case we would have no more than 10 μm for the operation. The glue would have to be driven in by capillary forces, and at the time we did not know anything about the viscosity of the conducting glue. The third option was a bit more appealing because it would give a direct contact to the gold electrodes, and give a larger contact area for the glue to stick to. The problem would be to remove a part of the lid without damaging the bonding or the gold layer. If a part of the lid would be removed, then we might as well use a more conventional method of connecting a wire, simply by soldering. By talking to different experimentalists at MIC, we learned that we could make a cut in the lid and then break a small part of the lid off.

3.2.3 Design of the electrodes

Due to the long microfluidic channel, a large number of electrodes had to be defined on the chip to obtain a large pressure. As stated in section 2.3 the pumping effect is inverse proportional to the spatial period of the electrode array, so the pumping effect should increase with miniaturization. The fabrication processes we had access to limited the minimum device feature size to five micrometer. We chose to make three different designs for the electrodes. In the smallest electrode design the large electrode was 30 μm wide, the small electrode was 5 μm wide and the gap between them was 5 μm. The spacing between the electrode pairs was the same as in Browns experiments, around 20 μm. We made a design where we changed the scale of the entire design, and a design where the
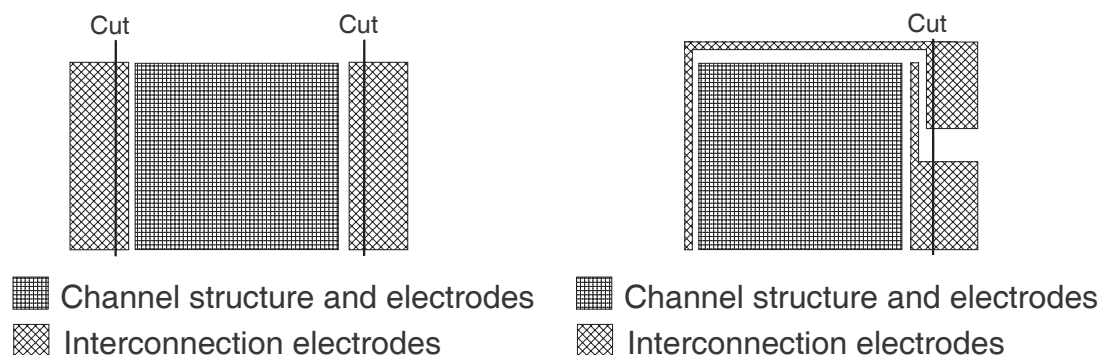
(a) The first draft for the design of the electrodes. The large interconnection electrodes are placed on each side of the actual chip. This use a lot of space and requires two cuts in the lid.

(b) The second draft for the electrode design. The large interconnection electrodes are placed on the same side of the chip, saving space and decreasing the need to make cuts in the lid. One of the large interconnection electrodes are connected to the other side of the chip by a wire.

Figure 3.2: The two drafts for the electrode design. One of the problems was how to place the two large interconnection electrodes.

ratio between the large and the small electrode was changed. The chips were referred to as S-G-L, where S is the width of the small electrode, G is the gap between the small and the large electrode, and L is the width of the large electrode. The dimensions for each chip design is listed in Table 3.1. Our first idea for the large interconnection electrodes was to place one on each side of the chip. A draft can be seen in Fig. 3.2(a). This would mean that we needed to use space for external electrodes on each side of the chip design. We would also have to make two cuts in order to get access to the large interconnection electrodes. In order to save space we tried to shrink the interconnection electrodes, so both could be placed on the same side of the chip. This would reduce the area of the chip, and we only had to make one cut. A draft can be seen in Fig. 3.2(b).

The chips were individually labelled with a number indicating the electrode geometry and its position on the wafer. The numbering can be seen in Fig. 3.3(a)

3.3 The final design

When the design of the electrodes and the microfluidic channel was done, we combined the two designs and the design of the chip was done. The design can be seen in Fig. 3.4. In order to reduce the stress induced in the SU-8 during processing, arrays of 100×100 μm holes, called stress relieving holes or stress holes, where we had large areas on SU-8. A stress reducing approach similar to this has been proposed by H. K. Chang and Y. K. Kim

Chip	10-10-60	10-10-30	5-5-30
Width$_{\text{large electrode}}$, L	60 μm	30 μm	30 μm
Width$_{\text{small electrode}}$, S	10 μm	10 μm	5 μm
Gap, G	10 μm	10 μm	5 μm
Spacing	35 μm	35 μm	20 μm
No of electrode pairs per chip	1030	1410	2000

Table 3.1: The specifications for the three types of chips. The difference between the chips lies in the electrode design and therefore only the electrode parameters are included.
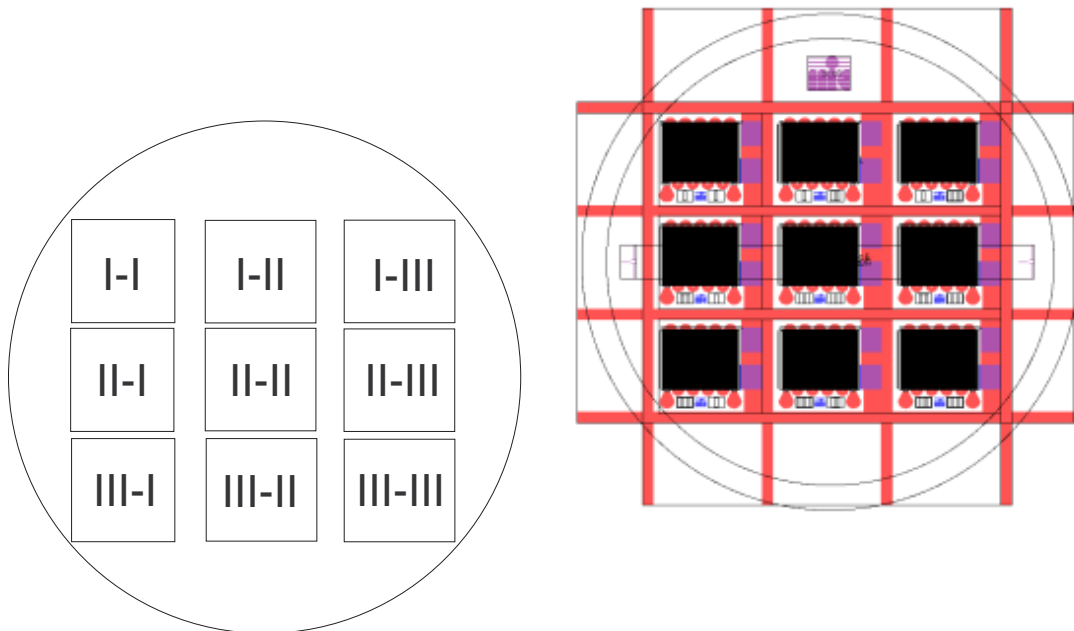
(a) The distribution of the chips on the wafer. We were able to place nine chips on each wafer and each chip was individually labelled, so we could keep track of each of them. The numbers shown in the figure corresponds to the numbering used in the design.

(b) Top view of the two masks designed. The red areas are for the SU-8 structure and the blue structures are gold electrodes.

Figure 3.3: Two views of the wafer. (a) is a schematic showing the placing of the individual chips and (b) is a mask design from L-Edit.
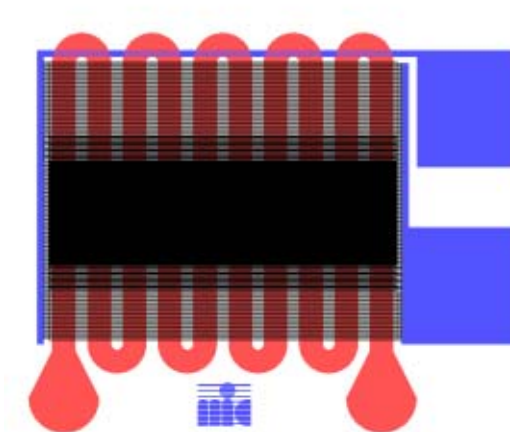
Figure 3.4: The final design of the chip. The figure is taken from L-Edit. The SU-8 structure is red, the electrodes are blue, and where SU-8 is on top of the gold layer, the color is purple. The two large interconnection electrodes are to the left, the inlet and outlet are placed in the bottom. Between them the labelling of the chip and the MIC logo are placed.

[5].

3.4   Calculations of expected performance of the pump

By using the dimensions from the design we were able to calculate the expected performance of the chips using the model proposed by Brown *et al.*. As explained in sec. 2.4, the flow induced above the small electrode is negligible, and therefore the velocity above the large electrode is used for the calculations. We used a Mathematica notebook produced by Anders Brask. The notebook can be seen in Appendix A. The velocity profile is linear through the liquid, with the average velocity at the bottom of the channel and a velocity of zero at the top of the channel. We obtained the theoretical values for the flow rates and pressures shown in Tables 3.2 and 3.3. The values for the flow rates of the 50 μm chips are, as expected, five times larger than the values for the 10 μm chips. The largest theoretical value of the pressure produced by the micropump is 1132 Pa.

Chip	$\langle v_{\mathrm{DL}} \rangle [\frac{\mu\mathrm{m}}{\mathrm{s}}]$	flow rate $[\frac{\mu\mathrm{L}}{\mathrm{h}}]$	Δp [Pa]
10-10-60	30	0.26	214
10-10-30	155	1.42	1132
5-5-30	60	0.54	429

Table 3.2: The expected flow rates and pressure drops for the three chip designs with 10 μm channels.

Chip	$\langle v_{\mathrm{DL}} \rangle [\frac{\mu\mathrm{m}}{\mathrm{s}}]$	flow rate $[\frac{\mu\mathrm{L}}{\mathrm{h}}]$	Δp [Pa]
10-10-60	29.78	1.30	9
10-10-30	157.18	7.10	45
5-5-30	59.56	2.70	17

Table 3.3: The expected flow rates and pressure drops for the three chip designs with 50 μm channels.

Chapter 4

Fabrication of the micropumps

In this chapter we describe the fabrication process of the micropumps. All processes except for bonding and dicing were carried out in the cleanroom at MIC to prevent dust from disrupting the electrode arrays. In the cleanroom we prepared the glass substrate, made the metal electrodes, the SU-8 polymer channels and the glass lid. The dimensions of the electrodes are so small, that dust may short circuit the arrays, making the pump useless.

4.1 Metallization

The substrate on which the pumps are fabricated, was a 500 μm thick pyrex glass wafer with a diameter of a 10 cm. The first fabrication step was a standard glass rinse on a rotating cleaning plate with de-ionized water and soap to remove any contamination of the wafer.

4.1.1 Lithography for electrodes

To make the photoresist adhere better to the substrate, a thin layer (10 nm) of aluminum was deposited (MICs Alcatel) prior to spinning. Spinning and prebaking of resist was done in the Karl Süss spinner. The resist, AZ5214E, was spun for 10 s at 2000 rpm and then for 20 s at 1000 rpm. A diagram of the wafer with resist can be seen in Fig. 4.1. Lithography was done in the Karl Süss aligner. We used contact mode and exposed the resist for 3 s
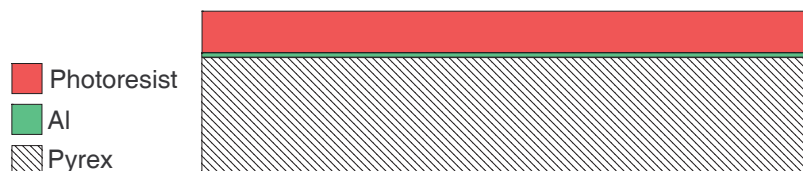

Figure 4.1: Side view of the glass wafer with a 100 μm thick layer of aluminum and a 1.5 μm thick layer of resist.
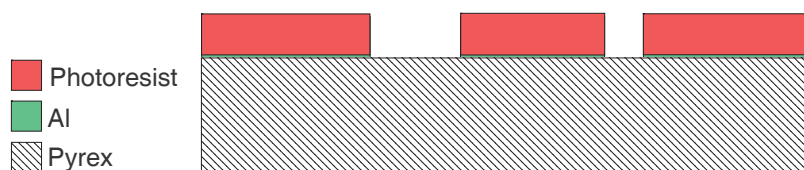
Figure 4.2: Side view of the wafer with aluminum and resist after lithography and development. The resist is removed where we want the gold to be deposited.
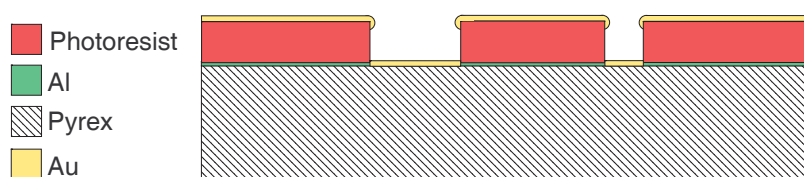
Figure 4.3: Side view of the wafer after deposition of a 10 nm layer of titanium (not shown) and of a 400 nm layer of gold. The titanium will act as a kind of glue between the gold and the glass wafer.

with ultraviolet radiation. This was followed by a post exposure bake for 100 s at 120 °C, and finally a float exposure.

Development of the resist was done in a AZ351B(NaOH) solution for 45 s. Afterwards the wafer was lowered into de-ionized water with agitation by means of N_2 bubbles. A diagram of the wafer at this step is shown in Fig. 4.2. The developer also removes the layer of aluminum.

4.1.2 Metal deposition for electrodes

The adhesion of gold to pyrex glass is not very good, therefore a thin (10 nm) layer of titanium is deposited. Titanium adheres well to glass and to gold, making it perfect as a link between the two materials. This method is quite convenient because it is possible to deposit the titanium and gold in the same machine. The layer of titanium is not shown in the fabrication diagrams. Subsequently the gold was deposited in a 400 nm thick layer covering all of the wafer surface, except for the sidewalls of the resist as can be seen in Fig. 4.3.

4.1.3 Lift off

To obtain the electrode arrays, we removed the remaining resist which was covered with gold. The lift off process was done by lowering the wafer in an acetone bath with ultrasound for approximately 10 min, resulting in structures as shown in Fig. 4.4. The resist was dissolved by acetone, and ultrasound made cracks in the resist shaking small pieces of half dissolved resist off, thus speeding up the process. Afterwards the wafer was flushed in

Figure 4.4: Side view of the wafer after lift-off. The resist has been dissolved and the gold deposited on top of the resist has been washed away. The gold left on the wafer defines the electrodes.

deionized water to remove any remaining acetone. This was important because the wafer was put into a bath with developer (NaOH) to remove the aluminum which re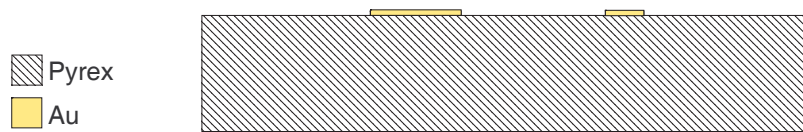mains on the chip. If any organic solvent comes in contact with the developer, it will start a powerful chemical reaction which is not desirable in a cleanroom.

4.1.4 Problems with lift off

We had some problems with lift of errors where the gold was not completely removed between the electrodes. This happened for seven of our chips. After consulting a research assistant we came to the conclusion that the lift off errors was caused by impurity of the acetone bath. A clean acetone bath will improve the lift off process.

4.2 Fabrication of microfluidic channels

The microfluidic channels was made in SU-8. SU-8 was perfectly suited for this purpose, as it allows high aspect ratios. It is also a very forgiving material with regard to a number of fabrication parameters, such as exposure times and etch times.

4.2.1 Annealing

The adhesion and uniformity of SU-8 to glass are dependent on the degree of hydration of the glass. If no dehydration of the glass has taken place prior to spinning, the SU-8 will not adhere very well to the glass, and the surface uniformity is not very good. Good surface uniformity are required for the structure because we want to close the channel with a lid. Any non-uniformity will cause the channels to leak. Therefore the wafers were annealed for at least 24 h at 120 °C before any processing can begin.

4.2.2 Lithography for microfluidic channels

The SU-8 was applied to the substrate by a standard spin method, using the Karl Süss spinner. The SU-8 was applied to the wafer manually by pouring, until approximately half of the wafer was covered with polymer. This is a quite large amount of polymer, but it ensures that enough SU-8 had been applied to the wafer. Then the wafer was spun at 500 rpm for 10 s, and then at 3000 rpm for 30 s. We had decided to make channels of two different heights. The method for doing so was a combination of choosing the right type of

Step	Ramp time	10 μm		50 μm	
		T_{target}	Plateau time	T_{target}	Plateau time
1	10 min	65 °C	2 min	60 °C	7 min
2	10 min	95 °C	2 min	90 °C	5 min
3	0	25 °C	until wafer reaches RT	25 °C	until wafer reaches RT

Table 4.1: The three steps in the SU-8 prebake procedure. Ramping times, temperatures and the plateau times are listed. The prebake was made on the hotplate. RT means room temperature.

SU-8 layer height	10 μm	50 μm
Exposure time	60 s	5 × 20 s, 10 s wait
Alignment gap	30 μm	80 μm
Exposure gap	30 μm	30 μm

Table 4.2: Parameters for the SU-8 lithography process for 10 μm and 50 μm thick SU-8 layers, respectively. Lithography was done on the Karl Süss aligner.

SU-8, and spin parameters. We made channels with heights of 10 μm and 50 μm. For the 50 μm structures we used a SU-8 called 2035. It was spun at 2250 rpm for 30 sec. After dismounting the wafer from the spinner, it was carried to a heating plate while keeping it as horizontal as possible, in order to keep the surface even. The wafer was placed on the heating plate, and prebaked such that the dissolving agent in the SU-8 evaporated, making it firmer and less viscous. To prevent cracks in the SU-8 due to uneven thermal expansion, the heating was ramped using the ramp times and temperatures listed in Table 4.1.

Following the prebake, lithography was done using the Karl Süss aligner. The parameters used are listed in Table 4.2. Due to an accident, one of the wafers was exposed twice. However, this overexposing should not result in a poor SU-8 structure as it is very hard to overexposure the SU-8 polymer. The channels of that wafer turned out to be just fine. After exposing the wafers were postbaked with ramp times and temperatures as listed in Table 4.3. This was done to evaporate the dissolving agent.

Development of the SU-8 layer was done in three steps, each one by lowering the wafer into a bath with the developer during magnetic stirring. The times and type of developer are listed in Table 4.4. The wafers were dried just by letting the isopropanol drip off and evaporate in the fumehood. This finished the fabrication of the bottom wafers, and they
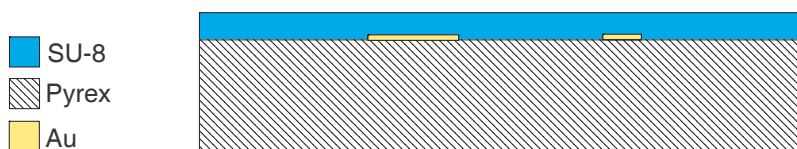

Figure 4.5: Side view of the wafer after the SU-8 layer has been spun on.

Step	Ramp time	10 μm		50 μm	
		T_{target}	Plateau time	T_{target}	Plateau time
1	10 min	65 °C	2 min	60 °C	5 min
2	10 min	95 °C	15 min	90 °C	35 min
3	0	25 °C	until wafer reaches RT	25 °C	until wafer reaches RT

Table 4.3: Ramping times and temperatures for SU-8 postbake, the postbake was done at the hotplate.

	First	Final	Rinse
Developer	First PGMEA	Final PGMEA	Isopropanol
Developing time 10 μm	2 min	2 min	3 min
Developing time 50 μm	90 s	90 s	5 min

Table 4.4: Parameters for Development of SU-8. The development was done with PGMEA and Isopropanol in a fumehood.

were put aside for bonding.

4.3 Bonding lids on the chips

The chips must be equipped with a lid which closes the channels. The lid consists of a pyrex glass wafer identical to the one, that the channels were produced on.

4.3.1 Preparation of the lid

The glass wafers was cleaned with a standard glass rinse. Then the wafers were dehydrated by annealing for at least 24 h at 120 °C to ensure good adhesion between the PMMA and the glass. The wafers were manually placed and aligned on the spin plate. We manually placed approximately 6 mL of PMMA on the center of the wafer taking care no bubbles were created, as this would affect the PMMA layer and disrupt the bonding. The wafers
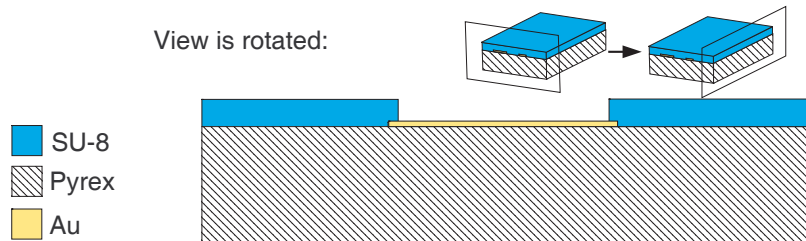

Figure 4.6: A rotated side view of the wafer, after the SU-8 layer has been developed. The microfluidic channels are produced in the development and are now visible for the eye. The hight of the SU-8 is 10 μm or 50 μm.
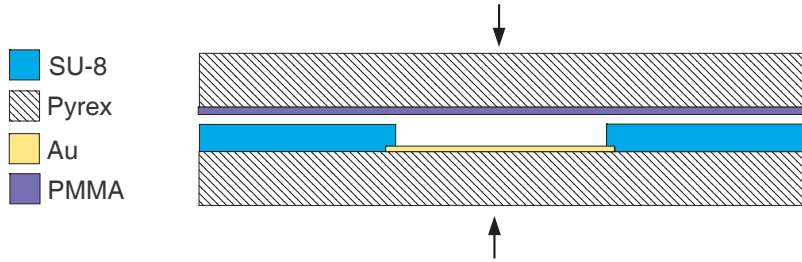
Figure 4.7: The two wafers are prebonded by hand. We place the wafer with the channels on a clean table and then carefully place the lid wafer on top of it. They were gently pressed together.

were spun at 2000 rpm for 60 s. Afterwards the wafers were baked for 10 min at 150 °C to remove the solvent in the PMMA. We used 950 kM PMMA in a 13% anisole solution.

4.3.2   Bonding of wafers using Thyra

The bottom and top wafers were assembled and pressed together by hand in the cleanroom as shown in Fig. 4.7, and put into cassettes. This ensured that no dust would get into the channels once outside the cleanroom. The bonding was done in Thyra, a machine customized to press wafers uniformly together with great force and simultaneously heating the wafers, making the formation of bonds more likely. The process takes place in a vacuum chamber. The vacuum was necessary in order to remove any air pockets between the two wafers. Due to the small space between the two wafers, the pressure has to be lowered slowly, otherwise the two wafers could be separated if the air expands to fast. The two assembled wafers were placed on the bottom plate between the designated pins while a dummy wafer was placed and fastened with pins on the upper plate as shown in Fig. 4.8. The chamber was closed and locked, and it was pumped to a pressure below 10^{-2} bar. Simultaneously, the heating plates were heated to 150°C. When both target temperature and pressure was reached, the plates were pressed together for 10 min. When the wafers had been pressed together, the plates were cooled with nitrogen gas until separation temperature had been reached. The wafers were removed at a temperature of 50°C, which should be sufficient for PMMA and SU-8 to bond. The pressure in the hydraulic system was 7 bar, corresponding to a bonding force of, 2000 N. Thus the pressure on the wafer was 2.5 bar.

4.3.3   Bonding problems and re-bonding

Immediately after the wafers had been unmounted from Thyra an inspection showed that Newton rings had been formed between the lid and the SU-8 structure on many chips. The Newton rings indicated that the bonding of SU-8 to PMMA had not been successful. Many of the chips were leaking when we tried to introduce liquid through the channel. We suspected that non-uniformity of the SU-8 layer was the cause of the leaks. For the chips

Assembled glass wafers

Heating elements

Pins

Dummy wafer
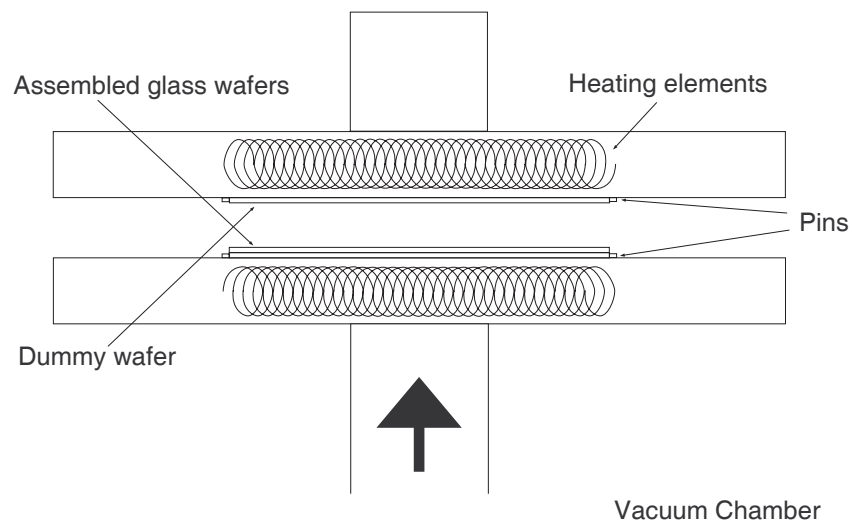
Vacuum Chamber

Figure 4.8: Sideview of the wafers placed in the vacuum chamber of the wafer assembling machine Thyra. The two wafers are held in place by movable pins on the bottom plate. A dummy wafer is pinned on the upper plate. The temperature of the plates can be raised by the heating elements and cooled by nitrogen, the nitrogen inlets are not shown on the figure. When the pressure in the chamber and the temperature is correct, the two plates are pressed together by hydraulic pistons.

that were leaking, we removed the lid and tried to re-bond them to obtain sealed structures. For the 50 μm chips we spun a double layer of PMMA in order to compensate for the lack of uniformity in the SU-8. We only used 50 μm chips for this method as we expected that the channels in the 10 μm chips would be filled by the thick PMMA layer. The chips were manually placed on the PMMA coated wafer and inserted into Thyra as described above. After bonding it was clear that the double layer of PMMA did not improve the bonding. Newton rings still appeared, making the pumps leak. Still, we were confident that a tight bonding could be obtained using the right parameters for the bonding. The same procedure was performed with another set of chips. This time the bonding time was increased to 20 min. to give the PMMA polymer more time to flow and thereby sealing the channel structure. Unfortunately no improvement was observed.

4.4 Final chip fabrication steps

To be able to make measurements on the chips, it was necessary to cut them out of the wafers. This procedure, called dicing, was carried out on a microsaw capable of cutting glass with a cut width of 0.5 mm. Furthermore in- and outlet holes had to be drilled, to make it possible to fill the channel of the pump with liquid.

4.4.1 Dicing the wafers into chips

The wafers were cut into chips 1.8 × 2.5 cm in size. Then a cut was sawed in the lid as shown in Fig. 4.9, making it possible to break off the glass so the interconnection electrodes were revealed. The depth of the cut for the first batch of wafers was 425 μm. Due to non-planar alignment of the saw, the cut was too deep for some of the chips, so that the interconnection electrodes on the bottom wafer was cut over. We reduced the cutting depth to 375 μm for the second batch, which eliminated the problem.

4.4.2 Drilling of in- and outlet holes

The in- and outlet holes were drilled with a high speed drilling machine, using cylindrical diamond drills, with flat heads. The chip was placed in a low glass beaker and covered with water. We used a small drill that could be moved up and down by hand. The chips were inspected in a microscope to determine if the correct depth of the hole had been reached.

4.5 Assessment of production methods

One of the big problems in this project has been the short circuiting of the electrode arrays. In Table 4.5 it is possible to se an overview of the production. The table shows that after production we had nine chips left that were not short circuited, but six of those were leaking and thereby not functional. The four chips that were broken beyond repairs, were broken in the initial stages of the production, either during drilling or when we tried to mount them in the setup.
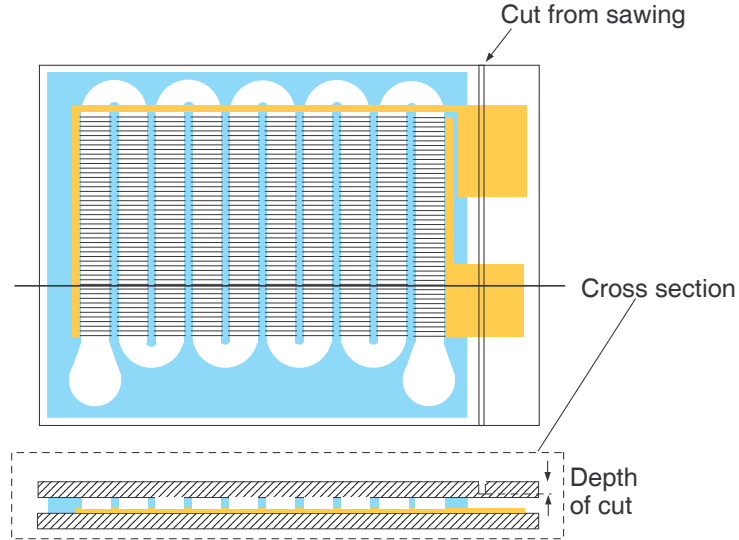
Figure 4.9: Top view and cross sectional view of a single chip, that has been diced. The figure illustrates how a deep cut through the lid over the interconnection electrodes has been sawed. This makes it possible to break off a part of the lid, and makes the electrodes accessible.

Total production	36
Short circuit	21
Broken beyond repair	4
Missing	2
Leaking	6
Net result	3

Table 4.5: An overview of the number of chips resulting from the production after the last fabrication step. 21 of the 36 chips contained a short circuit, leaving nine chips left after the production. Six were leaking and unable to function, giving a net result of three functional chips.

Reason for short circuit	No. of chips
Lift off failure	7
Bonding	5
Dirt	5
Unknown	4

Table 4.6: Overview of short circuit reasons. The chips with short circuits were examined in a microscope, and in most cases we were able to determine the reason for the short circuit.

The different reasons for the short circuiting of the chips are listed in Table 4.6. The chips that short circuited were inspected in a microscope, and in most cases it was possible to determine the cause of the short circuit. We detected a large amount of lift off failures resulting in contact between the two electrode arrays. We also detected a fair amount of damage from the bonding process. During bonding the two wafers sometimes moves a bit relative to each other and thereby causing stress in the structure between the wafers. For our wafers, we were able to see how the gold electrodes had been twisted beneath the SU-8 layer. Five of the chips had a short circuit due to dirt. They had been exposed to the unclean environment outside the cleanroom. For the remaining four of the short circuited chips we were not able to determine the cause of the short circuit.

The other big problem in the production was the poor bonding. 25 of 36 chips fabricated were leaking. One of the wafers simple lost the lid the first time it had been bonded, and two subsequent attempts to rebond the wafer was unsuccessful.

Chapter 5

Experiments and results

This chapter describes how the work with obtaining measurements was carried out. The different types of setups are described, and the problems associated with them are considered. The results are listed and commented.

5.1 Work procedures

In the laboratory we used a consistent approach to the experimental work during most of the project. All the chips were labelled with a color and a number to keep track of them. Before we mounted the chip in the setup, we always measured the resistance of the chip in order to determine whether it was short circuited or not. Then we mounted the chip, and measured the resistance again. We then filled the chip with liquid and connected the Lock-in amplifier. We made the observations we could, and if it was possible we made some measurements. The measurements were done at frequencies scanned from 500 Hz to 6000 Hz.

5.2 Determining the resistance and the capacitance

We used a Lock-in amplifier as a voltage source to drive the pump. The Lock-in amplifier is not capable of delivering very high voltages, but calculations, done in Sec. B.1, showed that the resistance of the liquid between an electrode pair was three orders of magnitude larger than the resistance of the electrodes. This would ensure that the voltage drop across the liquid would be high. So the Lock-in amplifier would be able to drive the pump. The Lock-in amplifier can measure the amplitude of the input signal, and the phase difference ϕ, between the out- and input signal, allowing calculation of the impedance of the micropump.

As described in section 2.4, the pump contains both resistive and capacitive properties, and thus it can be modelled as a serial connection of a resistor and a capacitor. A diagram of the equivalent circuit can be seen in Fig. 5.1 A serial connection of a resistor and a capacitor has an impedance Z, of

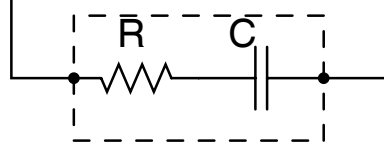$$Z = R + i\frac{1}{\omega C}.$$ (5.1)

Figure 5.1: Diagram of the electrical properties of our pump. The pump is modelled by a serial connection of a resistor and a capacitor. The pump is inside the dashed box.

of which the modulus $|Z|$ and the phase angle ϕ are given by

$$|Z|^2 = \left(\frac{1}{\omega C}\right)^2 + R^2 \quad \text{and} \quad \tan(\phi) = \frac{1}{\omega C}\frac{1}{R}. \tag{5.2}$$

From this we obtain

$$|Z|^2 = \left(1 + \left(\frac{1}{\tan(\phi)}\right)^2\right)\left(\frac{1}{\omega C}\right)^2. \tag{5.3}$$

By straightforward algebra C is found to be

$$C = \frac{1}{\omega|Z|}\sqrt{1 + \frac{1}{\tan^2(\phi)}}, \tag{5.4}$$

and from Eq. (5.1) we see that

$$R = Re[Z] = |Z|\cos(\phi) \tag{5.5}$$

In order to connect the Lock-in amplifier to the pump, a box was made with two cables connected to the Lock-in amplifier, and two contacts for connecting the pump. A diagram of the box can be seen in fig. 5.2 Using this setup, we made measurements on a R C circuit to test the equipment, and the test was successful.

5.3   Different types of setups

The setups used for measurements are described in chronological order to illuminate the iterative process of making an effective setup. Considerations on the setup includes several things including

- A tight sealing of the interconnection of the tubes to the in- and outlet holes is required.

- It should be possible to observe the channels through an optical microscope.

- The tubes connected to the in- and outlet channels should be placed equally high to prevent back pressure caused by gravity.

We used different types of liquid in the pumps, but mainly it was a 1 mM solution of $Na_2B_4O_7$ or "borax". In order to detect movement, we added fluorescent latex particles to the liquid. When the system was observed under a microscope, while exposed to ultraviolet light, any movement of the latex particles would be easily observed.
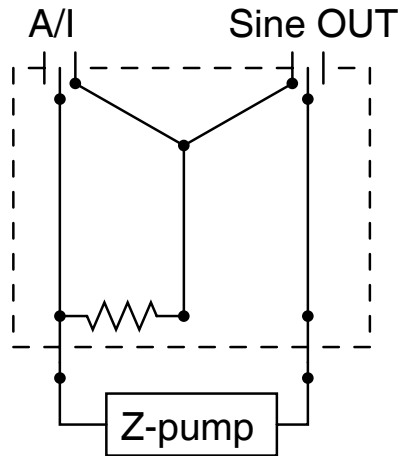
Figure 5.2: The schematics of the connection box between the Lock-in amplifier and the pump. The connection box is shown as a dashed line. Inside the box the circuit diagram is shown and the exits are marked "A/I" and "Sine OUT" according to their labels on the Lock-in amplifier. The resistor inside the box has a resistance of 50 Ω.
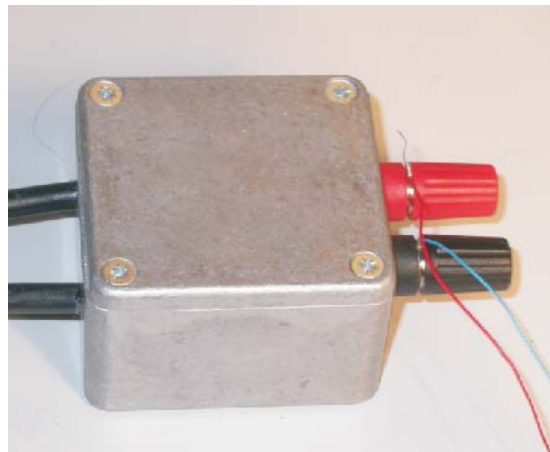
Figure 5.3: The grey box connecting the coax cables and the wires to the chip. The metal casing was for shielding noise and for connecting the Lock-in amplifier to the chip.
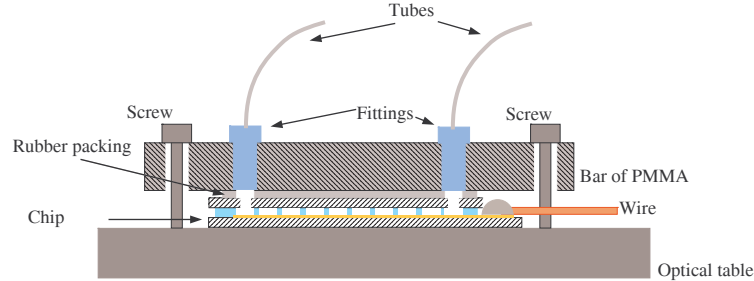
Figure 5.4: The figure shows a cross section of the first setup we used in the project. The liquid enters the chip trough the fitting. The fitting made it difficult to see what went on underneath it.

5.3.1   The first setup

The setup is shown in Fig. 5.4. It is the only setup where in- and outlet holes were drilled from the topside of the chip. For this setup we made a rubber packing and a bar with two threads and two holes in it. The threads were for the fittings that would connect the in- and outlets with two tubes. The holes were for the screws that kept the chip, rubber packing and bar together. A rubber packing was placed on the chip and the bar was placed on top of it. The sandwich of the chip, rubber packing and bar was aligned, ensuring that the holes in the bar matched with two screws sitting in the optical table. Two bolts were used to tighten the sandwich. The bolts should be tightened carefully otherwise the chip could break.

When the chip was mounted in the setup, the external connections were made. The inlet tube was connected to a syringe pump and a pressure sensor. The outlet tube was placed at the same height. The syringe pump was used to pump liquid into the chip at a constant flow rate to obtain measurements of the hydraulic resistance of the channels.

Problems

With this setup we broke a few chips, because we tightened the bolts to much. This caused the chip to bend, and eventually break. If the bolts were not tightened enough, the packing did not seal properly, and leakage occurred. Furthermore the bar made it a little difficult to see exactly what was happening at the inlets and outlets of the chip, because the fittings were placed right on top of them.

5.3.2   The second setup

To avoid any equipment on the top side of the chip, we drilled in- and outlet holes from the bottom of the chip. For the fluid interconnections a small PMMA substrate was made with two channels inside. The channels go in at the side, make a 90° turn upwards and
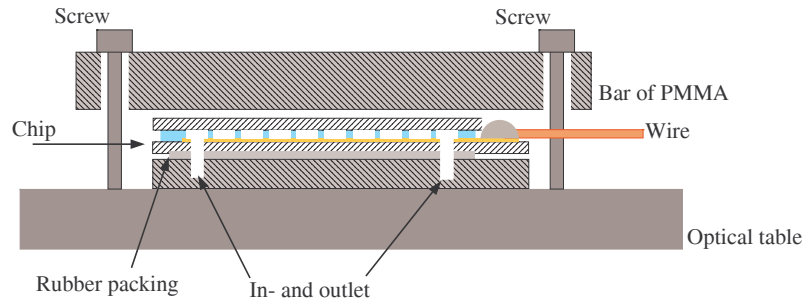
Figure 5.5: The figure shows a cross section of the second setup we used in this project. The liquid enters the chip from underneath trough the holes in the chip. In this setup it is very easy for us to see what is going on. The tube for the external circuit is glued to the side of the substrate because we expected high pressures.

exits the substrate at the top. The teflon tubes were glued to the substrate to avoid leaks. This setup allowed us to se when the rubber packing was tight, and we could examine the inlet and outlet during operation. This setup proved to function quite well. We could see all of the channel in the chip, including the inlet and outlet. We could see when the packing was tight enough and the setup was fairly easy to prepare.

5.3.3 The third setup

Unfortunately we did not obtain any pumping effect from the few micropumps that were bonded properly. This motivated us to try a different approach to observe the pumping effect. Therefore we decided to remove the lid from the chips. The SU-8 layer was still intact. A small drop of liquid containing buffer and latex particles was carefully placed in a single channel. Unfortunately, no movement was observed, and because the chip had no lid, the buffer quickly vaporized.

Problems

The problem with this setup, was the open nature of the chip, the liquid vaporized too quickly, for us to make a proper measurement. We needed another way of detecting the pumping effect where the liquid was confined in a channel.
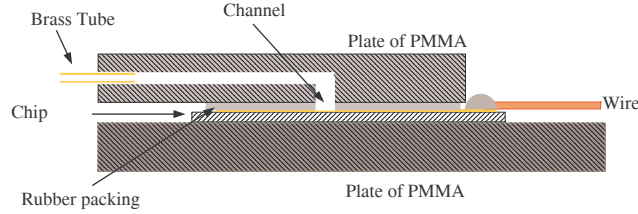
Figure 5.6: The figure shows a cross section of the fourth setup. The square piece of rubber with the channel was placed on the chip and aligned with an electrode array on the chip. The chip and the piece of rubber was placed between the substrate and a piece of PMMA. The sandwich was pressed together by two clips.

5.3.4   The fourth setup

To observe the pumping effect, we made a setup with just a single channel. In order to do so we removed the SU-8 from the chips with a knife, taking care not to scratch the electrodes. Using a CO_2 laser, we defined a 1 mm wide channel in a square piece of rubber. Instead of using teflon tubes, we glued brass pipes to the side of the substrate because we did not expect high pressures, and brass pipes are more easy to work with than teflon tubes. We placed the rubber structure on the chip and then placed the chip and the piece of rubber between the substrate and a piece of PMMA, in order to distribute the pressure from the clips evenly. We connected tubes to the brass pipes and filled the chip with buffer using a syringe. This setup proved to be very easy to prepare. We used two different rubber structures, one with a wide channel covering two electrode arrays and one with a more narrow channel covering only one electrode array. We also used rubber of two different thicknesses, 90 μm and 500 mum. The setup was easy to prepare, and worked well at low pressures. Furthermore it was easy to chance the geometry of our channel, by switching between different rubber structures.

5.4   Results

We did not obtain any measurements of the pumping effect, but we succeeded in measuring the hydraulic resistance of the chips with 50 μm SU-8 channels by measuring values of the flow rate and the pressure.

5.4.1   Hydraulic resistance

We were able to measure the hydraulic resistance of several of the 50 μm chips. As seen in Fig. 5.7 the different hydraulic resistances are quite similar, even for the laminated chip. In Table 5.1 we have a comparison of the theoretical values for the hydraulic resistance and the measured values. The measured values fits the theoretical values quite well with a deviation no larger than 25%. The be explained by that the calculation of the hydraulic

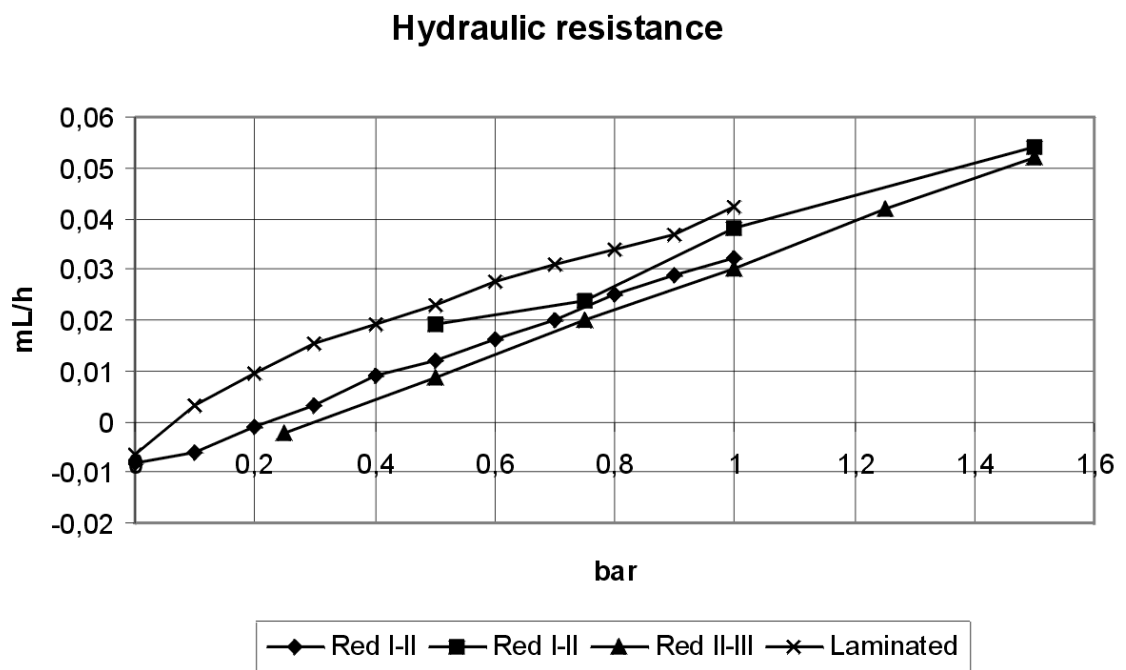Figure 5.7: The measurements of the hydraulic resistance. All the measurements were done on 50 μm chips. One of the chips had been bonded in the lamination machine and the rest are ordinary chips with a glass lid.

	Theory 50μm	Red I-II 1st	Red I-II 2nd	Red II-III	Laminated
$\frac{\text{m bar} \quad \text{h}}{\text{mL}}$	32.0	36.5	41.7	43.9	44.8
$\frac{\text{m bar} \quad \text{s}}{\mu \text{ L}}$	116	131	149	159	161

Table 5.1: Comparison of the theoretical value for the hydraulic resistance and the measured values. The Red I-II chip has been measured twice in order to recheck the measurements.

resistance does not take the turns of the meander channel into account. It is simply regarded as a straight channel. The calculation of the theoretical values of the hydraulic resistance is seen in Appendix E. Unfortunately we where not able to get steady flow of liquid through the 10 μm chips. Therefore no measurement of the hydraulic resistance could be obtained.

5.4.2 Indications of the pumping effect

In this project we have not been able to measure the pumping effect, but we have observed indications that motion occurred. We experienced a very slow flow with the fourth setup. In the microscope we could see the particles in the liquid move very slowly. Unfortunately the flow was too weak to be explained by the pumping effect. On the other hand we were not able to find any other explanation for the movement. It may have been caused by capillary pressure, but we do not think this is the case.

5.5 Further investigations of the experimental work

During the experimental work many issues came up, such as short circuiting of chips and formation of bubbles.

5.5.1 The buffer

It became clear that the buffer caused the electrical resistance of the chips to drop dramatically. This was not in accordance with the calculations we had done earlier, or with the results obtained by Brown *et al.* [2]. This resulted in that the Lock-in amplifier was not able to deliver high enough voltages to drive the pump. To investigate the problem a solution identical to the one used by Brown *et al.* [2], [4] was made. The solution was a 10^{-4} M solution of $NaNO_3$. This solution also caused the resistance to drop. Therefore there must be another reason for the short circuiting of the chips.

5.5.2 Formation of bubbles

The Lock-in amplifier was not able to induce electrolysis in the liquid on the chip. This was another indication that the resistance of the chips were lower than expected. By connecting another, more powerful, voltage source to the chip we were able to form bubbles in the liquid on the chips.
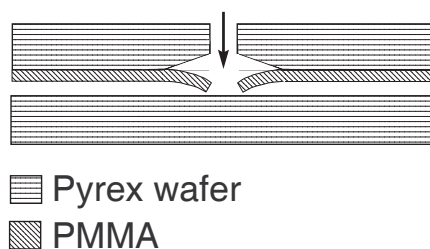
Pyrex wafer
PMMA

Figure 5.8: During the drilling some of the glass has broken off, the PMMA is still intact and is left hanging freely in the air, where it works as a valve when the liquid enters the chip. The flow of liquid is represented by the arrow going down into the hole.

5.5.3 Cleaning of short circuited chips

When the problem with short circuiting was as big as in this project, and when there was no time to produce new chips, it became important to clean the chips that had been short circuited during operation. The first approach was to clean the chips in ethanol and dry them with the compressed nitrogen supply in the laboratory. This method did not prove to be successful. Then we tried to combine a method where we used a strong base to dissolve whatever that was short circuiting the chips, followed by a sonic bath to help release dirt and sediments. None of the solutions worked entirely on their own, but the sonic bath seemed to be most efficient, especially if the chip had been soaked for 20 min in a basic solution before going to the sonic bath.

5.6 Problems

With the 10 μm chips we had a lot of problems getting liquid through the microfluidic channel. One reason for this could be that the inlet and outlet holes had been drilled from the top side. When the holes are drilled, the flexible PMMA on the bottom side of the lid is not removed, but hangs freely in the air, working as a valve. A model can be seen in Fig. 5.8. This can be avoided by drilling the holes from the bottom side of the chip. Throughout the project the small resistance of the chips had puzzled us. The calculation we had done showed that the resistance of the liquid was very large compared to the resistance of the electrodes. Then we noticed that we had only calculated the resistance of a single electrode pair, but these pairs was connected in parallel. This reduces the total resistance of the chip and as seen in Appendix B.3 the resistance of a chip is considerably smaller than we expected during the project. The calculated resistance is still much larger than the resistance we measured in the project. The only difference is that the measured resistance is not a factor of 100 smaller but only a factor of 4 to 10 smaller. With the new knowledge about the resistance of a chip it is clear that the Lock-in amplifier was not able to deliver enough output voltage in order to drive the micropump. Therefore a more powerful voltage supply is needed in order to use the design presented in this thesis.
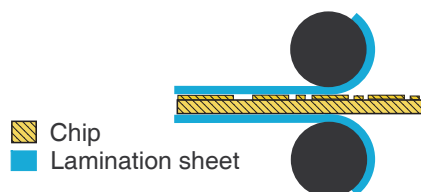
Figure 5.9: The lamination process. The chip is placed inside a lamination sheet and then it is driven trough the lamination machine, afterward the exceeding lamination sheet is cut away.

5.7   Bonding using lamination sheets

It has been proposed by M.O. Heuschkel, L. Guérin *et la.* [6] to use the polymer Riston® as a lid to microchips. We were keen to try this technique, as we had large difficulties with our regular bonding techniques. Unfortunately lack of time made it impossible for us to acquire some Riston® so we looked for something similar. At MIC a number of experimentalists have previously used a lamination sheet as bonding material with success. We decided to investigate this approach as well.

5.7.1   Experiments with laminated chips

By using a trial and error method we found that laminating a 50 μm chip with a standard lamination sheet required a temperature of 120 °C and the speed set to 6 on the machine. The lamination sheet had to go through the lamination process twice. With these settings the chip was able to hold tight, and there was no blocking of the channel. If the temperature was higher, the lamination sheets had been heated too much, that it had been in contact with the bottom of the channel and thereby blocked it. If the chip only went through the lamination machine once, then the bonding was not tight. This was also the case with a 10 μm chip, with the one exception - the lamination sheet had contact with the bottom and blocked the channels, i.e. the 10 μm structure was too low in order to prevent the blocking of the channel. During the experiments we did not find a set of suitable settings for bonding a 10 μm chip using a lamination sheet.

5.7.2   Method for laminating a chip

A chip with SU-8 structures is used. We turn on the lamination machine and apply the correct settings, T = 120°C and a speed of 6. The chip is carefully placed in a lamination sheet and inserted in the machine. No adjustments of the rollers inside the lamination machine is necessary. When the lamination is finished the sheet is allowed to cool off for a moment and then the chip is cut free with a scissor. The inlet and outlet holes are made with a sharp knife.

Chapter 6

Summary of problems and improvements

This chapter summarizes all the problems encountered during the work with the micropumps. We will also present improvements we think could solve the problems. In the end of the chapter we propose a three week project that will investigate the obvious improvements to the design and setup.

6.1 Short circuiting of the electrodes

The short circuiting of the electrodes was a crucial problem during the experimental investigation, as it causes the potential across the electrode pairs to drop, thus rendering the pump useless. The short circuiting was caused by several circumstances.

Lift off failure

When the electrode arrays were inspected using a microscope it became clear that, for many chips, the lift off process had been unsuccessful. Several of the electrode arrays were connected by small dots of gold. After a brief discussion with the laboratory assistant, it became clear that the reason for the incomplete lift off process was due to a unclean bath of acetone that should have dissolved the photoresist covered with gold. This problem should be avoided by using clean baths of acetone, when utilizing the lift off process. Another way to avoid the problem would be to use an etch process to define the electrodes, though compatibility between etching agent and the glass substrate should be considered.

Detaching of electrodes

The microscope inspection also showed that some of the electrodes had detached from the glass surface and now connected the two electrode arrays, thus causing a short circuit. It was observed that the phenomena only happened beneath the SU-8 structure. This indicates that, during bonding, the SU-8 structure is deformed, thereby causing stress in

the electrodes relative to the glass, resulting in detached electrodes. To prevent the stresses caused by the SU-8 layers, the bonding process should by carried out exerting great care.

Conductance of the liquid

We often experienced that the resistance of the chips dropped from infinity to a few hundred ohms when the liquid was introduced in the channels. Furthermore, no formation of bubbles by electrolysis could be obtained by adjusting the voltage using the Lock-in amplifier. In this project the Lock-in amplifier was originally intended as a voltage source, as it should be powerful enough to drive the micropump and thereby be able to induce electrolysis. These two things were very surprising since calculations done in the start of the project work, had shown that the resistance would be several thousands of ohms. Later this calculation proved to be faulty, as it did not take into account that the many electrode pairs are linked by parallel connection, thus lowering the total resistance of the chip as shown in Appendix B.3.

Deposition of dirt

After measurements had been done on a chip, the resistance had typically dropped as explained in the previous paragraph. But after the chip had been unmounted from the setup and dried, its resistance would still be only a few hundred ohms. This indicated that some conducting material had caused a short circuit in the electrodes. We were not able to determine exactly what was the cause, but we expect that minerals dissolved in the borax buffer had crystalized and formed a conductive link between the electrodes. This problem must be overcome if the micropump is to be integrated in a microsystem, and further investigations regarding the buffer must be made.

6.2   Leakage due to inefficient bonding

It was very surprising that the bonding that should enclose the microfluidic channels was as inefficient as it turned out to be. 25 out of 36 chips was so poorly bonded that the lid went off or leaks occurred. Prior to the fabrication we had consulted many process specialists for information on the bonding process. We got the clear impression that the bonding of PMMA coated glass wafers to SU-8 structures was an easy, high yield process. As it turned out, the poor bonding was very hard to overcome. A possible reason for the poor bonding could be that the wafers were removed from the bonding machine before they had cooled to room temperature, thus not making the bond strong enough. This was not the case though, as for the second batch of wafers, we waited until room temperatue before the wafers were removed. This did not improve the bonding. Another possible cause of the poor bonding is that the SU-8 layer was not uniform enough for the PMMA layer to adhere to. We were not able to determine how uniform the layer was, but it is clear that for a proper bonding the quality of the SU-8 layer is imperative.

We tried several methods for sealing the microfluidic channels. We tried adding superglue to the sides of the chip to let capillary forces drive it in between the PMMA and

the SU-8 structure, thereby sealing the channels. We also tried to rebond chips on which the lid had been removed, but to no avail. In the future, the bonding process must be evaluated to meet the requirements of a tight sealing of the microfluidic channels of the micropump. Another possibility is to use another method for the bonding process.

6.3 Introducing liquid into the microfluidic channels

We had problems getting liquid through the microfluidic channels of the chips and, as expected, especially the ones of a height of 10 μm. When we tried to inject liquid into the microfluidic channel the pressure started to build up, and eventually we had to stop the experiment or the lid might break off due to the high pressure. On most of the 10 μm the in- and outlet holes were made in the lid. This might have made the remaining PMMA work like a valve in the channel and thereby blocking the channel. Unfortunately the few 10 μm chips with the inlet and outlet holes in the bottom were leaking, so we were not able to obtain any results of the hyrdaulic resistance of the 10 μm chips.

The in- and outlet holes should be drilled from the bottom of the chip to avoid the valve effect of the PMMA layer. This also ensures that fittings connected to the in- and outlet, does not block the view to the microfluidic channels.

6.4 Improvements for the setup using the current design

With the design and the setups used in this project it has not been possible to detect the pumping effect. As seen in Appendix B.3 and mentioned in Sec. 5.6, the impedance of the chip is much smaller than expected. If the current design is to function more successful, then a more powerful power supply is needed and the grey box has to be redesigned. The bonding of the chip will still be a problem, but we have found several ways to avoid, or work around that problem in this project. One could simply skip the bonding and use a piece of rubber as microfluidic channel with a piece of polymer as lid, or the chip could be bonded in the lamination machine. Of course, none of the methods are optimal, but can be used for observing the pumping effect.

6.5 Improvements on the design of the micropump

In order to improve the micropump and making it work, a new design should be applied. The design presented in this thesis have several flaws. We tried to develop a micropump capable of delivering relative large pressures. To obtain this, the design was very ambitious having a long channel, and a large amount of electrode pairs, thus making the micropump more likely to short circuit. Furthermore, the impedance of the pump was too low for the Lock in amplifier to drive it. Finally the bonding was not tight enough for the microfluidic channels to contain the liquid.

A new design focusing on obtaining the pumping effect should consist of a straight channel, and an array of electrodes containing only one row as shown in Fig 6.1(a). This will decrease the number of electrode pairs, but will make it less likely that the chip will
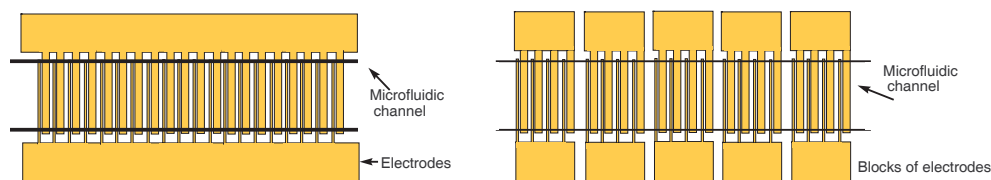
(a) The single row of electrodes should make the arrays less likely to short circuit.

(b) The blocks of electrodes can be disabled if one or more of the electrodes in the block short circuits. This makes it possible to pass by any short circuit that may occur.

Figure 6.1: Top view of two new pump designs with a single row of electrodes.

short circuit. Another possibility is to make the connection of the electrode pairs to the power source in blocks, making it possible to disconnect electrodes that short circuits as shown in Fig. 6.1(b). The latter method is only appropriate when making test systems for detecting the pumping effect as it requires enough space for the many interconnection electrodes. If the micropump should be integrated in a microfluidic system, there is no room for such a design. A more powerful voltage source should be used for driving the pump, to obtain voltages high enough for the effect to take place. Finally the walls of the microfluidic channel should be made wider, which should help to make the bonding more tight, thus preventing leakage in the chip.

6.6   Proposal for three week project

In this chapter we have come up with some improvements for the setup, i.e., a stronger power supply and a new grey box. The effect of these improvements could easily be investigated during a three week project. At DTU the last three weeks of each semester is dedicated to experimental work, where small groups of students carry out experimental work of scientific value. Due to the length of the period, the project are referred to as three week projects. Such a three week project could easily be made because the masks for fabricating the chip are in the cleanroom, the setup is made and only a stronger power supply is needed. The students participating in such a three week project will also experience problems with bonding, but we have found different ways to deal with this. We imagine a time schedule as:

First week The students will have a brief introduction to the theory behind the chip, and the chips are produced in the cleanroom.

Second week The students do experimental work in the laboratory, trying to detect the pumping effect.

Third week the students write a report about the project and make a presentation of their results.

It should be possible to carry out such a project within a three week period. A project like this would be a great opportunity to promote the research to new students who can carry on the work, that has been begun in this project.

Chapter 7

Conclusion

This thesis has presented the investigation of a novel design for an AC driven asymmetric electrode micropump. We have presented the theoretical background for asymmetric pumping devices. The general theory is derived from the work by Armand Ajdari [1]. The theory predicts a flow of liquid above an asymmetric surface. The flow is induced by an AC potential applied to electrodes on the surface, and is dependent on a phase difference between the impedance of the electrodes and the applied AC voltage. Furthermore, an analytical model for the flow generated by an asymmetric electrode micropump is investigated. The analytical model was originally proposed by Brown *et al.* [2]. The model assumed that the distance the ions move along the electrode surface is negligible, and that the field lines are of semicircular shape. The model is incomplete, and a satisfying model for the flow of liquid, requires further investigations into the nature of the flow of ions. It would be feasible to do this in FEMlab.

We wanted the pump to be able to deliver relatively high pressures. Therefore we chose to give the microfluidic channel a meander shape to obtain a long channel, and to concentrate a large number of electrode pairs on a single chip. The design was also made to investigate how the flow rate delivered by the micropump is influenced by the height of the microfluidic channel. Finally, three different designs for the geometry of the electrodes was made to investigate the effects of miniaturization. Unfortunately no pumping effect was observed.

The production took place in the cleanroom at MIC. The fabrication was carried out by us with the help of lab assistants. The production turned out to have a yield much lower than expected. The main reasons for the low yield was the poor bonding and lift off errors. We managed to work around the bonding problems by using a microfluidic channel made of rubber, but of course this method is only usable in a laboratory, and can not be used for integration in microfluidic systems. Unfortunately the chips tended to short circuit when the buffer was applied to the electrodes. During the project we found that the short circuit issue was not as dominant as first anticipated. Due to miscalculations in the beginning of the project we expected the impedance of the chips to be several thousands ohms, a correct calculation showed that the impedance was in the order of hundreds of ohms. This meant that the Lock-in amplifier was unable to deliver a voltage high enough

to drive the pump. A more powerful voltage supply should be able to drive the pump. Unfortunately it was the most important factors that turned out to be the problem in the project, other kinds of problems would not have had such a great influence on the project as the problems with the bonding and the short circuiting had.

We believe that the method of using AC driven asymmetric electrodes is a promising method for driving liquids in lab-on-a-chip systems. The problems we have had in this project can be overcomed by further research. The problems have been very educational and has given us a deeper insight in the important parameters when dealing with micropumps based on asymmetric electrodes.

Morten Arnoldus, s001604   Michael Hansen, s991279

Bibliography

[1] Armand Ajdari: *Pumping liquids using asymmetric electrode arrays*, Phys. Rev. E, **61**, 45-48 (2000)

[2] A. B. D. Brown *et. al.* : *Pumping of water with ac electric fields applied to asymmetric pairs of microelectrodes*, Phys. Rev. E, **63** , 016305-1 016305-8 (2000)

[3] Antonio Ramos, Hywel Morgan, Nicolas G. Green, Antonio Castellanos: *AC Electric-Field-Induced Fluid Flow in Microelectrodes*, Journal of Colloid and interfaces Science, **217**, 420-422 (1999)

[4] M. Mpolo, C.G. Smith, A. B. D. Brown: *Low voltage plug flow pumping using anisotropic electrode arrays*, Sensors and Actuators, **B 92** 262-268 (2003)

[5] Hyun-Kee Chang, Yong-Kweon Kim: *UV-LIGA process for high aspect ratio structures using stress barrier and C-shaped etch hole*, Sensors and Actuators, **84**, 342-350 (2000)

[6] M.O. Heuschkel, L. Guérin *et la.*: *Buried microchannels in photonpolymer for delivering of solutions to neurons in a network*, Sensors and Actuators, **B 48**, 356-361 (1998)

[7] Bent Elbæk *Bølger* p. 26, Niels Bohr instituttet 1997, 4. oplag, ISBN 87-87585-06-5

[8] Michael F Ashby, David R H Jones *Engineering Materials 1, second edition* p. 34 Butterworth-Heinemann, Oxford, ISBN 0 7506 3081 7, (1998)

[9] B. Helbo, A. Kristensen, and A. Menon *A Micro-Cavity Fluidic Dye Laser*, Micromechanics and Microengineering **13** 307-311

[10] Anders Brask *Principles of electroosmotic pumps*, Masterproject at MIC, February 2003, The Technical University of Denmark

Appendix A

Mathematica notebook used for velocity calculation

The mathematica notebook used for calculating the velocity above the large electrode.

Pumping using AC fields applied to asymmetric electrodes

This notebook is based on the work by A. B. D. Brown et al. Pumping of water with ac electric fields applied to asymmetric pairs of microelectrodes. Physical Review E, vol. 63, 2000.

Average Velocity above Electrode

■ Constants

```
ε = 80 * 8.854 10^-12;
σ = 1.23 10^-3;
λ = 30 10^-9;
η = 1 10^-3;
ω0 = 2 σ λ / (π ε);
```

■ Geometry and parameters

```
Φ = 0.8;
G = 10 10^-6;
S = 10  10^-6;
L = 60  10^-6;
k = L / S
xmin = G / (√k + 1 / √k);
xmax = (G + S + L) / (√k + 1 / √k);
```

6

■ Velocity above large electrode

Using the optimum frequency we find the velocity distribution above the electrode as function of position x. The average velocity agrees with A. B. D. Brown for the given parameters.

$$\omega = \omega 0 \Big/ \sqrt{xmax\, xmin}$$

$$f = \omega / (2\,\pi);$$

$$vL0 = \frac{6}{2\,\eta\,\sqrt{k}\,(1+k)^{\wedge}2};$$

$$p = \omega / \omega 0;$$

$$m = \frac{Log[k]}{\sqrt{k} - \frac{1}{\sqrt{k}}};$$

$$p1 = Function\Big[x, -\frac{vL0\,\Phi^{\wedge}2}{x}\,\frac{(p\,m\,x)^{\wedge}2}{(1 + (p\,m\,x)^{\wedge}2)^{\wedge}2}\Big];$$

$$pp1 = Plot\,[-10^{\wedge}6\,Evaluate[p1[x]], \{x, xmin, xmax\},$$
$$AxesLabel \rightarrow \{m, m/s\}];$$

$$vmean = -\frac{10^{\wedge}6}{xmax - xmin}\,Integrate[p1[x], \{x, xmin, xmax\}]$$

3350.85
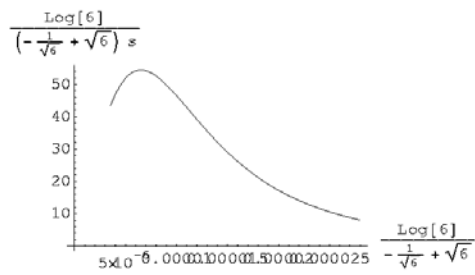
29.7807

Appendix B

Calculation of the electrical resistance in the chip

B.1 Comparing the resistance of the electrodes with the resistance of the liquid

We divide the gold electrodes into smaller, rectangular pieces of length $L_{\mathrm{electrode}}$, cross sectional area $A_{\mathrm{electrode}}$ in order to make the calculation easier. The electrodes consist of wide pieces and narrow pieces. The narrow pieces will be labelled R_{1-10} and R_{1-5} where the wide pieces will be labelled R_{2-60} and R_{2-30}. The second number in the subtext, is referring to the width of the electrode piece. The gap between the electrodes is filled with liquid and the resistance of these gaps are labelled R_{3-10} and R_{3-5}. The dimensions of the subelements are seen in Table B.1. The resistance is calculated using the well known formula for resistance

$$R = \varrho \frac{L_{\mathrm{electrode}}}{A_{\mathrm{electrode}}}, \tag{B.1}$$

	width	length	hight	Resistance
R_{1-10}	10 μm	1700 μm	400 nm	9.40 Ω
R_{1-5}	5 μm	1700 μm	400 nm	18.8 Ω
R_{2-60}	60 μm	1300 μm	400 nm	1.2 Ω
R_{2-30}	30 μm	1300 μm	400 nm	2.4 Ω
R_{3-10}	1000 μm	10 μm	10 μm	751880 Ω
R_{3-5}	1000 μm	5 μm	10 μm	375950 Ω

Table B.1: The dimensions used for calculation of the resistance. The resistance is only calculated for 10 μm chips, i.e., the hight of the conducting liquid. But the result will be used as an estimate for both 10 μm and 50 μm chips. The resistance of each part has been calculated and are listed in the last column

Chip	$R_{\text{electrode}}$	R_{liquid}
10-10-60	76.7 Ω	75188 Ω
10-10-30	106.7 Ω	75188 Ω
5-5-30	153.5 Ω	37595 Ω

Table B.2: Comparison of resistance in a single gold electrode with the resistance of the liquid between the electrodes.

width	length	height	Resistance
3000 μm	2500 μm	510 μm	1,22 10^6 Ω

Table B.3: The dimensions and resistance of the cavity between the two large interface electrodes. The resistance is so high that no significant current will flow.

where ϱ is the resistivity of the material. The total resistance of the gold electrodes will be the sum of five wide and five narrow electrode parts. The total resistance can be seen in Table B.2 where it is compared with the resistance in the liquid. The resistance of the liquid is divided by 10, as we consider it as a parallel connection of the 10 channels. The resistance in the liquid is much greater than the resistance in the electrodes, so it is reasonable to assume that the current will flow in the electrodes, so we can assume that the potential on the electrodes are constants through the hole electrode.

B.2 The resistance between the large interface electrodes

In our experiments we often have leaking chips, and we want to determine the resistance in the cavity between the two large interface electrodes, if it is filled with liquid. The dimensions of the cavity can be seen in Table B.3 were the resistance of the cavity is listed as well. The resistance is so high that no significant current will flow if the cavity is filled with water. Our electrical circuit is not influenced if the chip is leaking.

B.3 Determining the resistance of the entire chip

The chip can be considered as a lot of parallel connections. The resistance of each parallel connections are the same, and if the chip has N electrode pairs, then the resistance of the chip is determined by

$$R_{\text{system}} = \frac{R_{\text{electrode}} + R_{\text{liquid}}}{N}. \tag{B.2}$$

The total resistance of the chip can be seen in Table B.4

Chip	N	R_{system}
10-10-60	103	731 Ω
10-10-30	141	534 Ω
5-5-30	200	189 Ω

Table B.4: The total resistance of the chips. N is the number of electrode pairs on each chip.

Appendix C

Calculation of tube dimension for experiments

Using the Mathematica notebook we calculated that a 10 μm chip would have a flow rate of around 2 $\frac{\mu L}{h}$ or 2 $\frac{nm^3}{h}$. In order to be able to detect the flow, we observe how the fluid interface moves along a pipe. We want to be able to see the movement of the interface after approximately 10 min. To obtain this we need a tube of the right diameter d. In Fig. C.1 the interface at $t = 0$ and the interface at $t = 10$ min can be seen. The interface will move the distance $l_{\text{interface}}$ during the 10 minutes of operation, and have displaced an amount V_{tube} of liquid. The inner diameter d is determined by

$$d = \sqrt{\frac{V_{\text{tube}}}{l_{\text{tube}}\pi}} \tag{C.1}$$

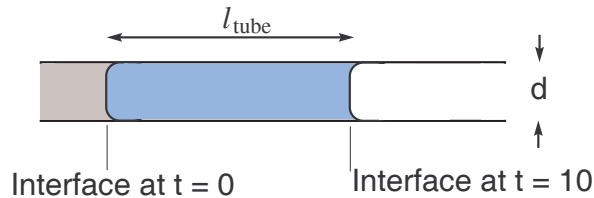The distance the fluid interface travels, and the corresponding inner diameter is listed in Table C.1

Figure C.1: Cross section of a liquid-gas interface in a pipe.

V_{tube}	l_{tube}	d
0.33 nm^3	10 cm	65 μm
0.33 nm^3	1 cm	103 μm

Table C.1: Calculation of tube dimension. V_{tube} is the volume of the crossed area in Fig. C.1, and l_{tube} is the distance we want the interface to move in 10 min. d is the inner diameter of an appropriate pipe, the calculation gives an idea of the diameter of the tube which allows easy observation of fluid movement.

Appendix D

Calculation of bending of the lid

During the first measurements, we had a lot of difficulties getting liquid through the microfluidic channels of the 10 μm chips. A possible cause of this was that the pressure from the bar on top of the chip in the measurement setup was pressing the lid down, causing it to bend and thereby block the inlet. Our supervisor, Anders Brask, has provided us with a formula for the bending of the glass

$$u = \frac{5}{384} \frac{p\, L_{\text{Lid}}^4}{E_{\text{young}}\, I} \tag{D.1}$$

where u is the the distance the glass is bending, p is the pressure applied, L_{Lid} is the length of the distance between the two edges of SU-8, E_{young} is Youngs modulus and I is the inertia. The formula is not an exact solution, but just a rough estimate. The inertia is

$$I = \frac{1}{12} L_{\text{Lid}}\, h^3 \tag{D.2}$$

where h is the thickness of the glassplate. By calculation I is found to be $31,25\,10^{-3}\text{mm}^4$. It is estimated that a pressure of approximately 1 bar is used when the chip is mounted in the setup. A pressure of 1 bar is equivalent to a pressure of $1\,\frac{\text{N}}{\text{mm}^2}$. We need to convert our
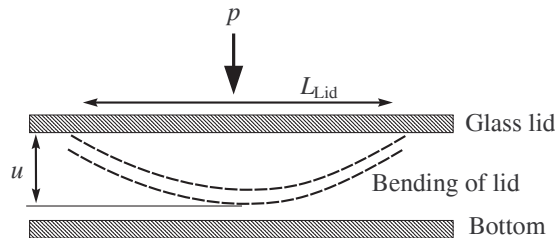

Figure D.1: The bending of the lid on the chip, due to the pressure in the inlet pipe. Pressure from the bar holding the setup together causes the lid to bend. The pressure is p, the length between the two edges of SU-8 is L_{Lid} and u is the distance the lid bends.

pressure from Newton per area to Newton per length. As the length of the unsupported lid is 3 mm, we get a pressure of 3 $\frac{\text{N}}{\text{mm}}$. Young's modulus is known from [8]. The bending of the glass is calculated to be

$$u = \frac{5}{384} \frac{3 \frac{\text{N}}{\text{mm}} 4 \, \text{mm}^4}{94 \frac{\text{kN}}{\text{mm}^2} \, 31,25 \, 10^{-3} \, \text{mm}^4} = 1,077 \, \mu\text{m}. \tag{D.3}$$

The glass plate will bend around 1 μm. This is not enough to block the channels, as they are at least 10 μm high. Therefore it is not likely that the problems with driving liquid through the microfluidic channels are caused by bending of the lid.

Appendix E

Determining the hydraulic resistance

The flow rate in a microfluidic channel is determined by

$$Q_{\text{total}} = Q_{\text{pressure}} + Q_{\text{pump}} \tag{E.1}$$

where Q_{pressure} is the back pressure flow rate and Q_{pump} is the flow rate generated by the micropump. Q_{pressure} is found as

$$Q_{\text{pressure}} = \int_0^h v(x)dx = \frac{1}{2}\frac{\Delta p}{L_{\text{channel}}}\left[\frac{1}{3}x^3 - \frac{1}{2}x^2 h\right]_0^h = -\frac{1}{12}\frac{\Delta p}{\eta L_{\text{channel}}}h^3 w \tag{E.2}$$

where h is the height of the channel, w is the width and v is the velocity profile shown in Fig. E.1. Δp is the pressure drop along the channel. Q_{pump} is

$$Q_{\text{pump}} = \frac{1}{2}V_{\text{slip}}wh \tag{E.3}$$

By setting $Q_{\text{pressure}} = Q_{\text{pump}}$ is is possible to find an expression for Δp. The calculation yields $\Delta p = v_{\text{slip}}wh$. The hydraulic resistance can be determined from

$$R_{\text{hyd}} = \frac{\Delta p}{Q_{\text{total}}}. \tag{E.4}$$

We determine the hydraulic resistance by measuring the pressure and flow rate. The spreadsheet used for the calculations are seen in Fig. E.2
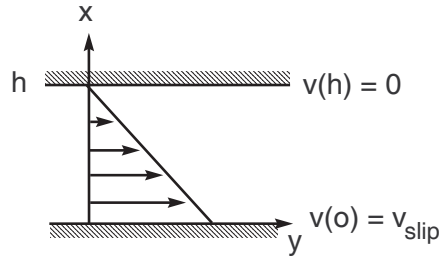

Figure E.1: The velocity profile for the micropump

Pumping with AC using asymmetric electrodes

by Anders Brask

Width (W)	Depth (D)	Length (L)	Pressure	Dyn. Visc.	Flow rate
mm	μm	mm	bar	kg/(m s)	μL/s
1	10	120	1	1,00E-03	6,94E-02
m	m	m	Pa		m^3/s
1,00E-03	1,00E-05	1,20E-01	1,00E+05		6,94E-11

Velocity	Flow Rate	Max pressure	cm H2O	μL/hr
μm/s	μL/s	bar		
29,3	7,33E-05	2,11E-03	2,1	0,26
m/s	m^3/s	Pa		
0,0000293	7,33E-14	2,11E+02		

Figure E.2: Spreadsheet used for calculation

Appendix F

Simulation in FEMlab

Due to the experimental nature of this project and the time allocated for it, we have only simulated a one dimensional system in FEMlab. In this appendix the equations governing the flow is stated and the result of the simulation is presented.

F.1   Setting up 1D simulation

The liquid contains two ion species of the concentrations c_1 and c_2. We begin by stating the continuity equation for the two species, and the Poisson equation

$$\dot{c}_1(x,t) + \nabla \cdot J_1 \quad = \quad 0, \qquad J_1 = -\alpha c_1 V' - D c_1', \tag{F.1}$$

$$\dot{c}_2(x,t) + \nabla \cdot J_2 \quad = \quad 0, \qquad J_2 = +\alpha c_2 V' - D c_2'. \tag{F.2}$$

where α is an arbitrary constant and J_1 and J_2 are the current densities of the species. The Poisson equation reads

$$\nabla^2 V = -\frac{\rho}{\epsilon}, \tag{F.3}$$

where the charge density ρ, is given by

$$\rho = (z_1 \frac{c_1}{N_A} - z_2 \frac{c_2}{N_A}) e N_A = (c_1 z_1 - c_2 z_2) F_{\mathrm{a}}, \tag{F.4}$$

and

$$F_{\mathrm{a}} = e N_A. \tag{F.5}$$

Eqs. (F.1) and (F.2) are first order in time, but to the second order in space. Eq. (F.3) is second order, therefore Eqs. (F.1), (F.2) and (F.3) are all second order equations. The boundary conditions of our system are

$$V(0) = \frac{V_{\mathrm{ext}}}{2}, \quad V(x_{\mathrm{L}}) = -\frac{V_{\mathrm{ext}}}{2}. \tag{F.6}$$

At the wall the electrical force equals the diffusion force.

$$\begin{aligned} J_1(0) = 0, \qquad J_1(x_{\mathrm{L}}) = 0 \\ J_2(0) = 0, \qquad J_2(x_{\mathrm{L}}) = 0. \end{aligned} \tag{F.7}$$
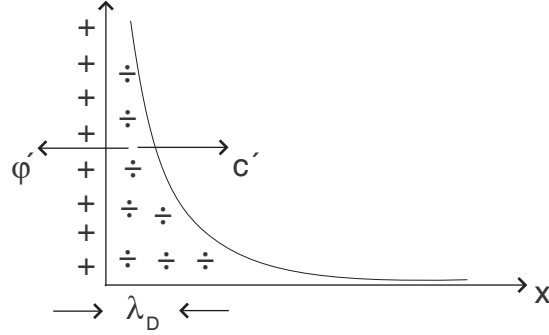
73

Figure F.1: The Debye layer in equilibrium. The electrical forces attracts ions to the wall and the high concentration of negative ions near the wall repulses some of the negative ions. Therefore the attractive and repulsive forces equals each other out. The Debye length λ_D is shown in the bottom of the graph

The initial conditions are

$$\left.\begin{array}{c} c_1(x, t = 0) \\ c_2(x, t = 0) \end{array}\right\} \quad = \quad c_0 \quad \Rightarrow \quad \rho(x, 0) = 0 \tag{F.8}$$

which gives

$$V_{\text{ext}}(x, t = 0) = V_{\text{ext}}(\frac{1}{2} - \frac{x}{x_{\text{L}}}). \tag{F.9}$$

The static solution is seen in Fig. F.1 where

$$\lambda_D = \sqrt{\frac{\epsilon k_B T}{2z^2 e^2 c}}. \tag{F.10}$$

F.2   Results of the simulation in FEMlab

The result from the simulation i FEMlab is seen in Fig. F.2. The initial conditions of the simulation is seen in Fig. F.2(a), as the simulation reaches equilibrium the charge has been swept away from the bulk and is located at the walls as seen in Fig. F.2(c)
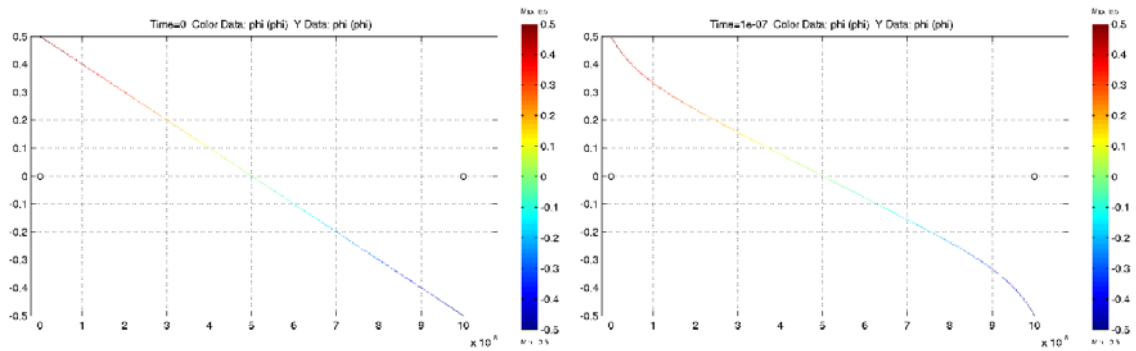
(a) The initial condition of the simulation, notice the linear potential across the bulk liquid.

(b) The simulation after two timesteps. The charge has just begun to build up at the walls, and the potential is slightly twisted at the walls.
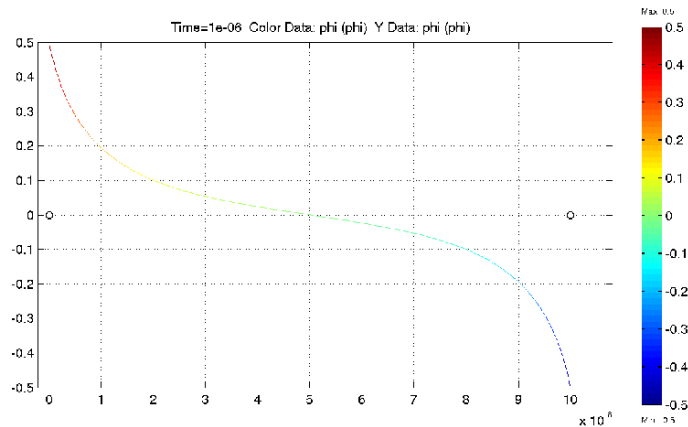
(c) The last step in the simulation, the solution to t equals infinity, and the charge is mainly located at the walls. The electric field is curved due to the high concentration of charge at the walls and is almost zero at the bulk.

Figure F.2: Three figures from the simulation. The initial step, a step in the beginning of the simulation and the last step in the simulation, i.e., the solution when t equals infinity